

Hematite spherules at Meridiani: Results from MI, Mini-TES, and Pancam

W. M. Calvin,¹ J. D. Shoffner,¹ J. R. Johnson,² A. H. Knoll,³ J. M. Pockock,¹ S. W. Squyres,⁴ C. M. Weitz,⁵ R. E. Arvidson,⁶ J. F. Bell III,⁴ P. R. Christensen,⁷ P. A. de Souza Jr.,⁸ W. H. Farrand,⁹ T. D. Glotch,¹⁰ K. E. Herkenhoff,² B. L. Jolliff,⁶ A. T. Knudson,⁷ S. M. McLennan,¹⁰ A. D. Rogers,¹⁰ and S. D. Thompson¹

Received 25 November 2007; revised 21 March 2008; accepted 14 May 2008; published 4 December 2008.

[1] We report on observations of hematite-bearing spherules at Meridiani Planum made using the Microscopic Imager (MI), Mini-Thermal Emission Spectrometer (Mini-TES), and Panoramic Camera (Pancam) instruments on the Mars Exploration Rover Opportunity. Spherules were observed on soil surfaces and in outcrop rocks, both on undisturbed surfaces and in abraded surfaces ground using the Rock Abrasion Tool (RAT). Spherule size and shape change little along the 850 m eastward traverse from Eagle Crater to Endurance Crater, but spherules decrease and then slightly increase in size along the 6 km traverse from Endurance south to Victoria Crater. Local populations range from submillimeters to several millimeters in diameter. An additional small diameter (100 μm) size population is possible. An increase in irregular shapes is found near Victoria Crater. This, combined with the size decrease south of Endurance, suggests either a changing depositional environment, or variation in the duration and timing of diagenetic events. The dominant smaller size population observed early in the mission in aeolian areas and ripple crests is observed as the primary size population in abraded outcrop farther south. This suggests that successively younger beds are exposed at the surface along the southward traverse. Stratigraphically higher units removed by erosion could be recorded by the present surface lag deposit. Coordinated systematic observations are used to determine optical and infrared hematite indices of the surface soils in Pancam and Mini-TES. In spite of the systematic variation seen in MI, both Pancam and Mini-TES indices are highly variable based on the local surface, and neither show systematic trends south of Endurance. The lack of a 390 cm^{-1} feature in Mini-TES spectra suggests concentric or radial interior structure within the spherules at scales too fine for MI to observe. Mini-TES does not detect any silicate component in the spherules. A bound water component in soils or in exchange with the atmosphere is observed. These spherules have been previously interpreted as concretions formed within what were once water-saturated, diagenetically altered “dirty evaporate” sandstone sediments. Our observations support this interpretation; however, no single terrestrial analog provides a model that can account for all attributes of the spherules on Mars.

Citation: Calvin, W. M., et al. (2008), Hematite spherules at Meridiani: Results from MI, Mini-TES, and Pancam, *J. Geophys. Res.*, 113, E12S37, doi:10.1029/2007JE003048.

1. Introduction

[2] Among the most interesting surprises at the Mars Exploration Rover Opportunity’s landing site on Meridiani

Planum was the observation that the signature of bulk hematite observed from orbit by the Mars Global Surveyor (MGS) Thermal Emission Spectrometer (TES) [Christensen *et al.*, 2000] was caused by a large number of small round

¹Department of Geological Sciences and Engineering, University of Nevada, Reno, Nevada, USA.

²U.S. Geological Survey, Flagstaff, Arizona, USA.

³Department of Organismic and Evolutionary Biology, Harvard University, Cambridge, Massachusetts, USA.

⁴Department of Astronomy, Cornell University, Ithaca, New York, USA.

⁵Planetary Science Institute, Tucson, Arizona, USA.

⁶Department of Earth and Planetary Sciences, Washington University, St. Louis, Missouri, USA.

⁷Department of Geological Sciences, Arizona State University, Tempe, Arizona, USA.

⁸Tasmanian ICT Center, CSIRO, Hobart, Tasmania, Australia.

⁹Space Science Institute, Boulder, Colorado, USA.

¹⁰Department of Geosciences, State University of New York at Stony Brook, Stony Brook, New York, USA.

Table 1. Microscopic Imager Summary of Observations Used in Size-Frequency Survey^a

Sol	MI Spots	Observed	Measured
010	1	1	1
012	1	1	1
014	3	13,11,13	20
015	2	4	4
017	2	7,3	6
019	1	3	3
022	1	4	4
023	1	13	5
039	4	2,4,1,3	8
040	1	1	1
042	1	1	1
046	1	15	11
047	1	25	13
048	2	1,35	16
049	1	6	6
050	1	1	1
052	1	30	11
054	2	6,18	8
063	1	45	7
069	1	9	6
073	1	26	8
080	1	18	12
084	1	50	9
085	1	15	10
086	1	1	1
100	1	15	6
105	1	35	13
106	2	30,18	23
122	1	11	2
124	4	2,3,2,2	6
125	1	1	1
142	2	3,1	4
144	1	5	1
145	1	3	2
146	1	1	1
148	1	1	1
158	1	5	4
164	1	2	2
174	2	1,2	3
176	1	2	2
177	3	3,11,6	16
181	2	1,1	2
182	3	6,5,3	14
186	2	2,6	8
212	2	1,2	2
221	3	4,13,9	20
235	1	5	5
239	1	1	1
244	3	1,6,2	9
257	3	2,7,1	10
258	2	1,2	2
259	1	3	1
Total	81		334

^a“MI Spots” notes the number of Microscopic Imager (MI) locations surveyed on a given Sol. For each location, the number of spherules observed in each frame is given along with the number of spherules measured.

grains covering the surface. In false color composite Pancam images, what are actually dark gray spherules in natural color RGB images [Bell *et al.*, 2004] appeared bluer than the surrounding soils, and so they quickly gained the nickname “blueberries” among the science team. Many observations were used to reveal the hematitic nature of these grains [Squyres *et al.*, 2004a, 2006a]. Initial analysis showed that the infrared spectral signature of hematite was

absent in airbag bounce marks where the spherules were depressed into the surface [Christensen *et al.*, 2004]. Pancam spectra of undisturbed soils showed a 900 nm absorption consistent with the presence of coarse gray hematite [Bell *et al.*, 2004; Soderblom *et al.*, 2004; Weitz *et al.*, 2006]. The Alpha Particle X-Ray Spectrometer (APXS) showed strong elemental lines of iron [Rieder *et al.*, 2004] and the Mössbauer Spectrometer (MB) data showed the characteristic Fe³⁺ sextet associated with hematite [Klingelhöfer *et al.*, 2004; Morris *et al.*, 2006].

[3] More detailed analyses confirmed the hematite contribution in numerous soils and in small grains on the surface of dune crests, and that the infrared spectral signature of hematite appears as an isolated end-member in spectral transformations, although bulk spherule composition as modeled from APXS suggests that there may also be a silicate component in these spherules [Morris *et al.*, 2006; Glotch and Bandfield, 2006; McLennan *et al.*, 2005; Jolliff *et al.*, 2007b]. More recent work suggests that a thin coating of dust may have the same effect as a nonhematite component on the APXS spectra but the available observations still cannot exclude an additional silicate contribution [Jolliff and the Athena Science Team, 2005; Jolliff *et al.*, 2007a; Knoll *et al.*, 2008]. On the basis of a number of factors, including their uniformity in size, their sparse three-dimensional distribution within outcrop rocks, their lack of concentration along bedding planes, the rare presence of doublets and still rarer triplets (i.e., joined spherules), and raised surface ridges surrounding some spherules that parallel depositional lamination in enclosing sandstones, the spherules are interpreted to be postdepositional concretions formed during groundwater diagenesis [e.g., Squyres *et al.*, 2004b; Grotzinger *et al.*, 2005; McLennan *et al.*, 2005]. This interpretation is consistent with the pattern of size variation observed in the long (~7.5 km) traverse to Victoria Crater and attributed to variation in the availability or composition of diagenetic fluids [Squyres *et al.*, 2006b]. One model of spherule formation suggests the spherules formed as acidic groundwater percolated through porous sandstones with precipitation driven by more neutral groundwater along a reaction front as seen in terrestrial environments [Chan *et al.*, 2004]. Alternate models are based on the observation that small hematitic spherules formed during hydrothermal alteration of a cinder cone on Mauna Kea, Hawaii [Morris *et al.*, 2005], and some have interpreted the spherules as accretionary lapilli during an impact base surge event [Knauth *et al.*, 2005]. Detailed consideration of these and other possible models is provided in section 7.

[4] Mission activities through Sol 511, the extraction of the rover from Purgatory ripple, are summarized by Squyres *et al.* [2006b]. This paper synthesizes observations of the spherules from the Microscopic Imager (MI), Panoramic Camera (Pancam) and the Mini-Thermal Emission Spectrometer (Mini-TES) instruments. Data acquired in the first ~1000 Sols of Opportunity’s mission include systematic coordinated observations using both Pancam and Mini-TES, Rock Abrasion Tool (RAT) grinds in outcrop, and directional Mini-TES scans across the plains. These observations were designed to constrain the interior structure, formation mechanisms and geologic/geochemical evolution of the

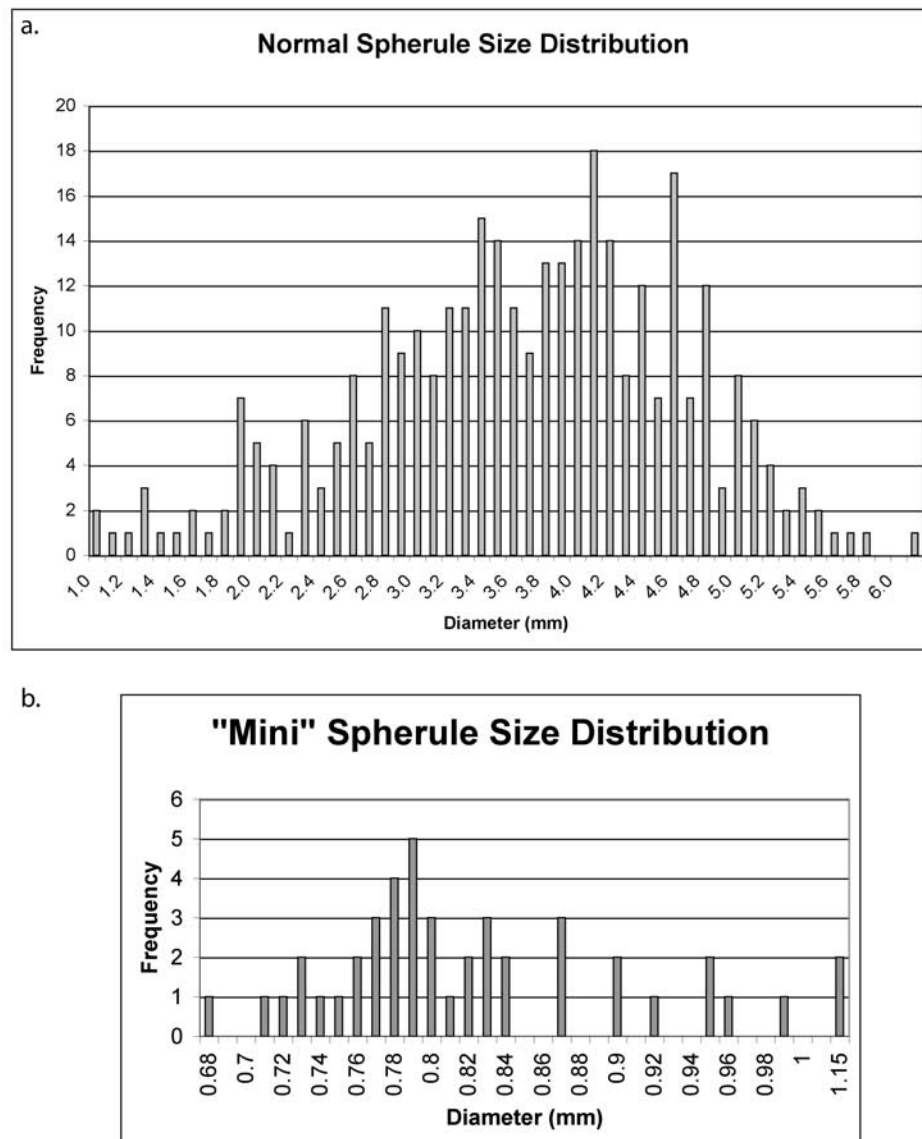


Figure 1. (a) Size-frequency distribution for Microscopic Imager (MI) images surveyed between Sols 10 and 260. A total of 81 image frames and 336 spherules were measured. See also Table 1. (b) Size-frequency distribution histogram of the small, “mini”-spherules observed in drifted material inside Eagle Crater on Sol 53. A total of 44 spherules in one MI frame were surveyed and range in size from 0.68 to 1.12 mm in diameter.

spherules. Specific information on the instruments and payload is provided by *Squyres et al.* [2003].

2. Size Distribution

[5] The spherules are ubiquitous, and between Eagle and Endurance craters are relatively uniform in size and tone [Soderblom *et al.*, 2004; Weitz *et al.*, 2006]. We surveyed 50 MI frames acquired between Sols 10 and 260 to determine the size frequency distribution of loose spherules sitting on the plains as well as some well exposed samples observed within outcrop rocks. Table 1 lists the Sol number, the number of different MI frames studied, the number of spherules and spherule fragments that were observed in

each frame, and the number for which we were able to determine good diameter measurements. In each spot we measured the spherules using the image in the MI stack that provided the best focus. For each MI frame, between 1 and 15 individual spherules were measured along three axes and averaged to determine the spherule diameter. In each case no broken, partial or buried spherules were included. Spherule diameter was measured in pixels and we used the pixel-scale conversion ($30 \mu\text{m}/\text{pixel}$) to convert to diameter in millimeters. Figure 1a shows the derived size frequency distribution for “normal-sized” spherules. The spherules show a Gaussian distribution around 3.7 mm diameter, with a range from less than 1 to 6.7 mm. The patch inside Eagle (“Vanilla” and “Cookies N’ Cream”

Table 2. Summary of Statistics for All Types of Nodules^a

Type	Number of Observations	Q1 (mm)	Median (mm)	Mean (mm)	Q3 (mm)	IQR (mm)	S.D. (mm)	CV (%)	CI99 (mm)
Mini	44	0.764	0.795	0.821	0.862	0.098	0.092	11.1	[0.785; 0.857]
Spherule	334	2.953	3.698	3.604	4.353	1.400	0.996	27.6	[3.558; 3.838]
Coated	37	3.510	4.004	3.926	4.240	0.731	1.078	27.5	[3.469; 4.383]

^aQ1 = first quartile (percentile 25); Q3 = third quartile (percentile 75); IQR = interquartile range (Q3–Q1), which is the interval containing 50% of the intermediate data, s.d. = standard deviation, CV = coefficient of variation given in %. CI99 = Confidence Interval of 99%. Coefficient of variation: $CV = 100 \times \left(\frac{\sigma}{\bar{X}} \right)$ where σ is the standard deviation and \bar{X} is the calculated mean. Confidence Interval: $CI_{99\%} = \bar{X} \pm 2.576 \times \left(\frac{\sigma}{\sqrt{N}} \right)$ where N is the number of observations.

observations on Sol 53) showed a distinctly smaller population and so these MI frames were counted separately. These small spherules have a mean diameter of 0.8 mm and range from 0.68 to 1.12 mm (Figure 1b and Table 2). Figure 2 and Table 2 show the statistical analysis of these measurements. Additional populations of small spherules (mean diameter of 1–2 mm) were observed on top of ripple crests [Weitz *et al.*, 2006]; these populations also include angular grains, interpreted to be spherule fragments, in addition to the smaller rounded spherules.

[6] During the exploration of Endurance Crater, spherules with overgrowths of sulfate-rich cement were observed (“batter berries”) at the lowest levels reached within the crater, and a collection was surveyed in MI images from Sols 194 and 199 (Figure 3). These coated spherules range in diameter from 1.8 to 6 mm, typical of uncoated spherules with coating thickness approximately 0.5 to 2 mm. The median of coated spherules is 0.4 mm larger than for “normal” spherules (Table 2). McLennan *et al.* [2005] interpreted the coatings as cements and observed that they may be as thick as 4 mm, but we cannot know whether all nodular cements have concretions at their cores.

[7] As Opportunity trekked south to Victoria Crater, soils were surveyed at sparse intervals. Soil observations up to Sol 552 (Reiner Gamma) are summarized by Weitz *et al.*

[2006] who documented a general decrease in size in spherule size along the traverse. Later soil and ripple observations are similar. Unusual new spherule shapes were noted and are discussed in section 3.

[8] In the Sols leading up to our arrival at Victoria Crater (Sol 951), Opportunity performed 28 RAT grind operations in outcrop rocks that sliced through 91 individual spherules (Table 3). Because of motor stalls in the shoulder azimuth joint of the instrument deployment device (IDD) (beginning on Sol 654), and the loss of the encoder on the RAT grind motor (Sol 1045) the frequency of IDD operations has decreased. New methods were established for grinding after the RAT encoder failure, allowing grinding of the Cercedilla Outcrop near the margin of Victoria Crater (Sol 1178). In RAT holes in outcrop the number of spherules increases and the size decreases with distance south of Endurance (Table 3 and Figures 4 and 5) [Squyres *et al.*, 2006b; Weitz *et al.*, 2006]. Table 3 presents the number of spherules seen in each RAT grind hole. For a more complete view of later Sols, we include two targets that were only brushed and not ground, because of the hardware constraints noted above. Figure 4 shows examples of changes in size observed in MI images and Figure 5 presents a summary of the size of spherules measured in each RAT grind. To determine size we again took several diameter measurements of each

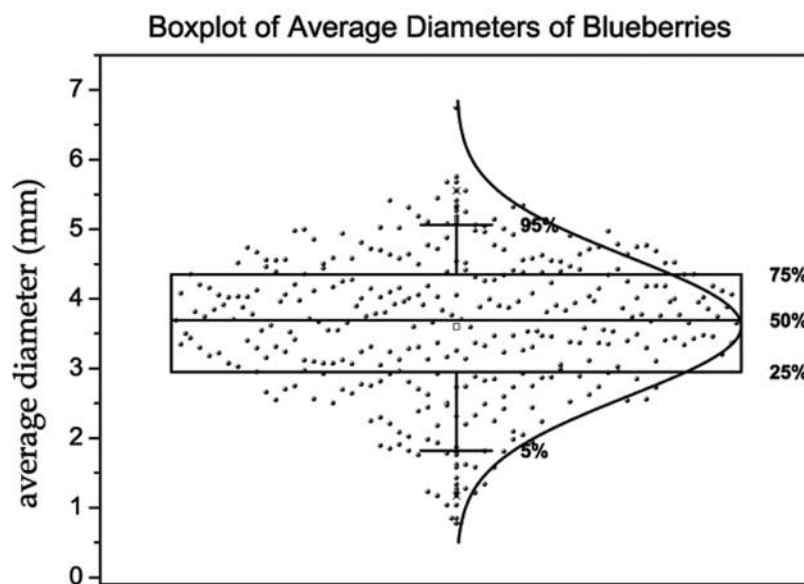


Figure 2. Box plot size frequency distribution of spherules used to determine size range statistics in Table 2. Each point is one measurement and the box denotes the median, Q1 (25%), and Q3 (75%) confidence intervals. See also Table 2.

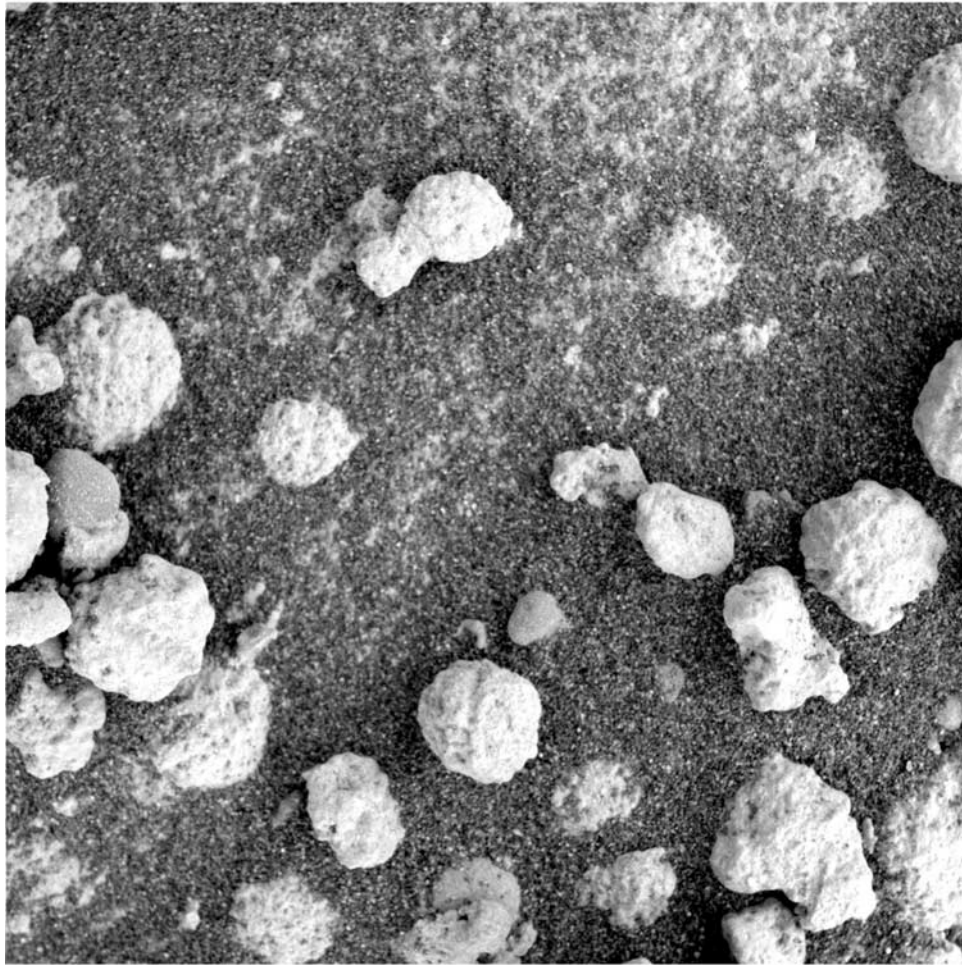


Figure 3. MI of coated spherules inside Endurance Crater. Image 1M145851010EFF3505P2936M2M1 acquired on Sol 199. Full MI frame is 3.1 cm wide.

exposed spherule and averaged the values, similar to methods described above. Size estimation of spherules exposed by RAT grinding is not straightforward. Because spherules are generally not sectioned through their centers, these measurements reflect lower limits. Accordingly, differences among spherules could in principle reflect actual size differences or different cuts through spherules of equivalent size. For this reason, multiple measurements in a single sample cannot be interpreted simply as size variation for the population they represent, and only the largest measured diameters may approximate true spherule size. Nonetheless, the observed differences between in situ spherules before and after Sol 300 (Figure 5) are significant and systematic and thus are unlikely to be sampling artifacts. They corroborate observations from loose soil spherules that average size decreases along the traverse from Endurance to Victoria craters. This also supports the idea that the hematite spherules are lag deposits generated locally. Pancam observations of outcrop surfaces also show an absence of larger spherules between Erebus (about 3.6 km south of Endurance) and Victoria craters. Two of the observations are of brushed outcrop tops only (Sols 1035, “Rio de Janeiro” and 1168 “Cape of Good Hope”), and these will underestimate the true size of spherules. An estimate of total spherule

volume (also a lower limit) in these RAT grinds suggests that the total volume also decreases.

[9] The size of spherules in RAT holes observed in Eagle and Endurance craters is consistent with the general survey of the sizes in soils (Figure 1). The small spherules on top of drift material in Eagle and on plains ripples (Figure 2) may be fragments of larger spherules that have been transported. However, they are also consistent with the smaller size population seen in outcrops farther south. Spherules as small as 0.2 to 0.3 mm have been observed in both undisturbed and ground outcrop. As seen in Figures 4e and 5, the rock target Cercedilla (Sol 1182) is unique in having both a larger (>2 mm) and very small (<0.5 mm) spherule examples. The Cercedilla target is similar in color to larger blocks Madrid and Guadarama, interpreted as possible ejecta blocks from lower within Victoria Crater. In the Cercedilla RAT hole, there are two large spherules, one ground through at the edge of the hole, and the upper surface of another remained intact. Very small spherules, consistent with small size seen elsewhere, occur in the interior of the grind as shown in Figure 4e.

[10] In one RAT hole (Sol 546, Figure 6) hundreds of dark spots of order 2 to 6 pixels, 60 to 180 μm appear in the MI images. These spots are similar in size to the smallest

Table 3. Spherules in RAT Holes^a

RAT Hole	Location	Sol	Spherules	Comments	Mosaic ID
McKittrick	Eagle 30, 33	30	2	no mosaic, best single frame	1M130859552EFF0454P2959M2M1
Guadalupe		34	3	no mosaic, best single frame	1M131212854EFF0500P2959M2M1
Flatrock		45	0	no mosaic, and MB nose print, 1? Upper rt?	1M132180521EFF05A6P2959M2M1
Bouncerock		67	0		1MM_067BOUNCE_RAT_HOLE
Pilbara	Fram	87	1		1MM087ILF14PER09P2936M222M1
Lionstone	Endurance Rim	108	1		1MM108ILF22PER22P2956M222M1
Tennessee	End. Interior	139	1		1MM139ILF31PER82P2956M222M3
Cobble Hill		145	0		1MM145ILF31PER90P2957M222M2
Virginia		146	0		1MM146ILF31PER90P2907M222M3
London		149	2		1MM149ILF31PER90P2906M222M1
Grindstone		152	0		1MM152ILF32PER00P2977M222M1
Kettlestone		154	0		1MM154ILF32PER00P2977M222M1
Drammensfjorden/Millstone		162	1		1MM162ILF32PER21P2977M222M1
Diamond Jenness		177	1	178(ratted farther no berry)	1MM177ILF33PER36P2907M222M1
Mackenzie/Campbell		184	0		1MM184ILF33PER70P2907M222M1
Inuvik		188	0		1MM188ILF34PER12P2957M222M1
Axel Heiberg/Bylot/Atineq		195	0		1MM195ILF35PER05P2957M222M1
Escher		219	1		1MM219ILF35PERBGP2956M222M1
Paikca/Whatanga	Endurance	306	1		1MM306ILF38PEREVP2956M222M2
Gagarin/Yuri	outside Vostok	403	6		1MM403EFF50PER00P2956M222M2
One Scoop/Ice Cream		546	16		1MM546ILF58PER47P2957M222M2
One Scoop/Ice Cream		549	0	reacquire One Scoop	1MM549ILF58PER47P2936M222M2
Strawberry	Fruitbasket	558	0		1MM558ILF58PERDIP2936M222M2
Lemon Rind		560	0		1MM560EFF58PERDIP2936M222M2
Olympia/Kalavrita	Erebus	633	43		1MM633ILF64PER00P2936M222M2
Rimrock/Ted	Erebus	691	0		1MM691ILF64PERKCP2936M222M1
Baltra	Beagle	894	4		1MM894ILF74PERV1P2937M222M1
Cha	Outside Victoria	962	3	no mosaic, best single image	1M213586802EFF76POP2936M2M1
Rio de Janeiro		1035	6	brush only, no mosaic	1M220066778EFF77UNP2936M2M1
Cape of Good Hope		1168	8	brush only	1MMB68ILF82PER0TP2936M222M2
Cercedilla		1182	5	grind	1MMB82ILF82PER##P2936M222M2
Total Spherules:		91			

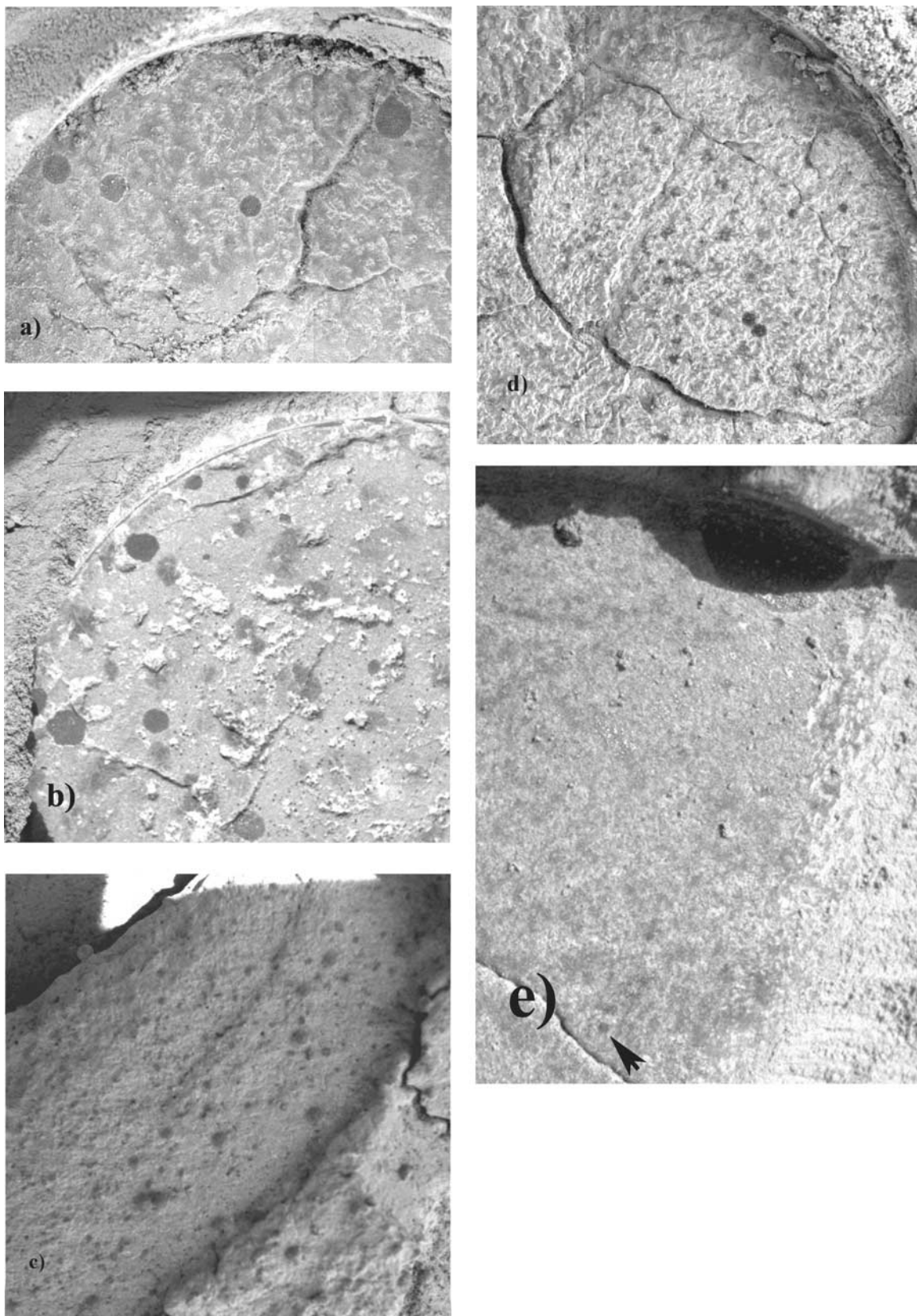
^aILF is an image mosaic produced by the MultiInstrument Processing Lab (MIPL) at JPL, typically a point perspective. EFF is an uncalibrated individual MI frame. The brushed only observations on Sols 1035 and 1168 are not included in the total. RAT is Rock Abrasion Tool.

dark spots seen in undisturbed outcrop at “Jerome,” Sol 649 (Figure 4c). The MI resolution is insufficient to resolve these smallest sand-size features. At least some spots appear to be etch pits or shadows, on the basis of their consistent appearance on the anti-illumination side of small-scale surface topography. However, many are not immediately explained by illumination effects. These spots may be basaltic sand grains (see, for example, background in Figure 3); alternatively, they may record a third spherule population of “microberries.” This interpretation is consistent with the appearance of numerous small berries in the Olympia/Kalavrita RAT grind target on Sol 633, just 250 m south of the Sol 546 “One Scoop” target [Squyres *et al.*, 2006a]. We note that the features are both sparse and distinctly isolated from each other. They are better resolved than any sand grains seen in MI’s of other soil or rock

targets. They also appear circular in cross section, within the limits of the instrument resolution. It should also be noted that the Mössbauer instrument (MB) has detected a strong (35%) hematite component in the outcrop rocks that is not associated with spherules [Morris *et al.*, 2006]. These potential micrometer-sized spherules may correspond to that hematite component (along with jarosite) observed in the sulfate matrix by MB.

[11] Although initial MI images suggested a bimodal distribution of spherule size, one group with diameters around several millimeters and a second group with diameters of 1 mm or less, the spherule observations up to Victoria Crater suggest a gradation in sizes, ranging from a few hundred micrometers to many centimeters diameter. The population may extend to very small sizes

Figure 4. Spherule size changes with distance from Endurance. (a) Target “Gagarin” at Vostok Sol 403. Image is 3 cm wide and spherules range from 1.4 mm (center) to 2.5 mm (upper right). (b) “One Scoop” north of Erebus, Sol 546. Image is 2.3 cm wide and the largest, darkest irregular spherules are 1.8 and 1.6 mm. (c) Small spherules in undisturbed outcrop Sol 649 (“Jerome”); the perched spherule in the upper left near the bright patch is <1.2 mm. Also note a number of small, disperse dark spots. (d) Very small spherules in Baltra, Sol 894; image is 2.7 cm wide, and dark adjacent spherules are ~0.8 mm in diameter. (e) Sol 1182 Cercedilla grind on the rim of Victoria Crater. Image is 1.2 cm wide and shows a large 2.8 mm spherule at the edge of the Rock Abrasion Tool (RAT) grind (in partial shadow), and the arrow points to a small 0.27 mm spherule just above the fracture. Images used in Figures 4a, 4b, 4d, and 4e are cited in Table 3; image in Figure 4c is 1M185797775EFF64BNP2957M2M1.

**Figure 4**

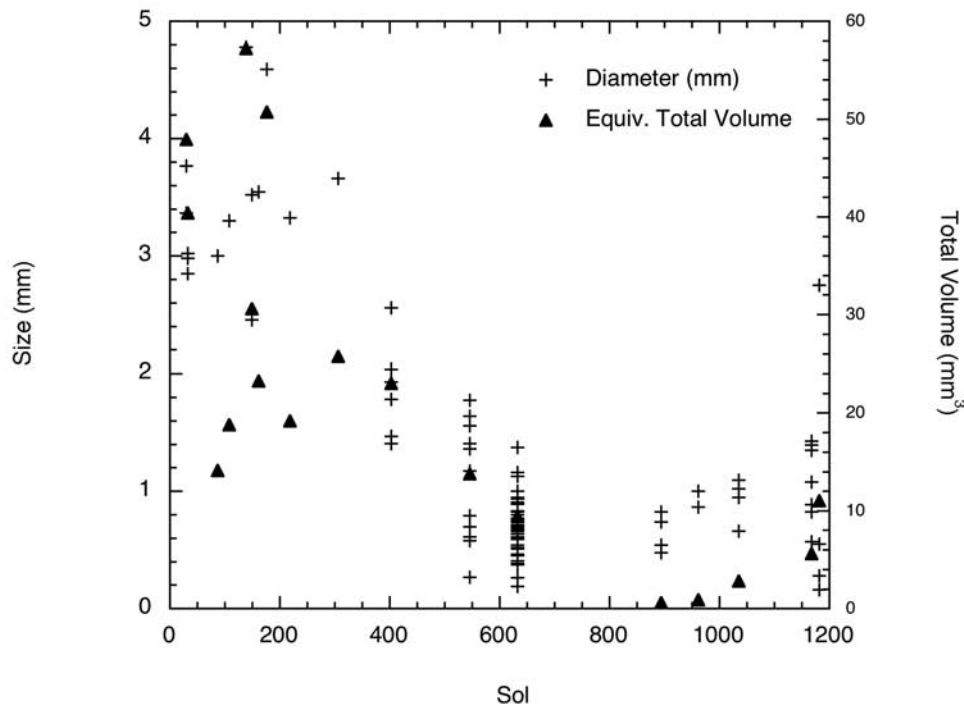


Figure 5. Size of spherules in RAT holes. Spherules become more frequent and smaller south of Endurance. Ceredilla (Sol 1182), a possible ejecta block from within Victoria Crater, is unique in having large and small sizes that overlap pre-Endurance and post-Endurance sizes. Sols 1035 and 1168 are brushed outcrop tops only. Equivalent total volume (mm^3) is the sum of all spherules assuming $4/3\pi r^3$ for the volume of an individual spherule.

of order $100 \mu\text{m}$, but these interpretations test the resolution limits of the MI.

3. Shapes and Interior Structure

[12] As noted by McLennan *et al.* [2005], the spherules, either in RAT holes or in broken sections on soils, are uniform in albedo and typically lack interior structure at the spatial scale of the MI. Knauth *et al.* [2005] showed two examples (from Sol 28 and Sol 142) that they interpreted as dark cored spherules. Such examples are exceedingly rare, and over the course of the mission there were very few examples of dark spherule interiors. In most RAT grinds, polishing of the larger spherules occurs in arcs because of the geometry of the RAT grind heads, and usually dark regions are parallel with polish striations on the spherule. This suggests that differences in surface roughness may lead to the appearance of dark cores due to RAT polishing. However, There is one example, on Sol 139 (Figure 7a), that shows grind polishing oriented perpendicular to the orientation of the darker interior. Another possible concentric interior was observed in a broken spherule on Sol 1216 (Figure 7b). None of the later spherules in RAT grind holes showed interior structure, though one broken spherule showed uneven fracture textures (Sol 1166, Figure 7c). In the target Cha, small spherules were observed to have a very thin coating of cement (Sol 962, Figure 7d).

[13] Very few odd-shaped or fused spherules were imaged prior to Opportunity's arrival at Victoria Crater. Examples of a few doublets and one triplet were illustrated by McLennan

et al. [2005, Figure 7] and Weitz *et al.* [2006, Figure 13] showed the one teardrop shaped example observed to date. Pronounced irregular shapes were first noted in the "One-Scoop" RAT hole on Sol 546 (Figures 4b and 6). A wide variety of forms in this single RAT hole include large, dark areas with slightly irregular surfaces, small, dark, circular patches and a number of intermediate, irregular patches. The darkest spherical shapes with clear boundaries between them and the surrounding matrix are interpreted as typical Meridiani spherules in a range of sizes. The irregular surfaces suggest that the diagenetic environment favored development of more clustered nucleation points and, therefore, fused forms. Lower porosity or increased compaction of matrix sediments would lead to nonuniform growth conditions and might result in fused rather than isolated spherule forms. Such forms may also indicate variability in spherule growth rate depending on local iron saturation in the outcrop. This situation is found in terrestrial environments where faster growing concretions overtake and incorporate smaller, slower growing ones [e.g., McBride *et al.*, 1999]. McBride *et al.* [2003] have argued for a pervasive growth model for calcite concretions in sandstones. Here, rather than a center outward growth model, precipitation occurs across the concretion area [e.g., Raiswell and Fisher, 2000]. If such growth is short-lived or stops, we envision that the precipitation would form shadows in which subtle tone and color alteration occurs without creating sharp boundaries with the surrounding matrix. The lightest toned "splotches" in the One Scoop RAT hole are interpreted as resulting from weaker concentrations of

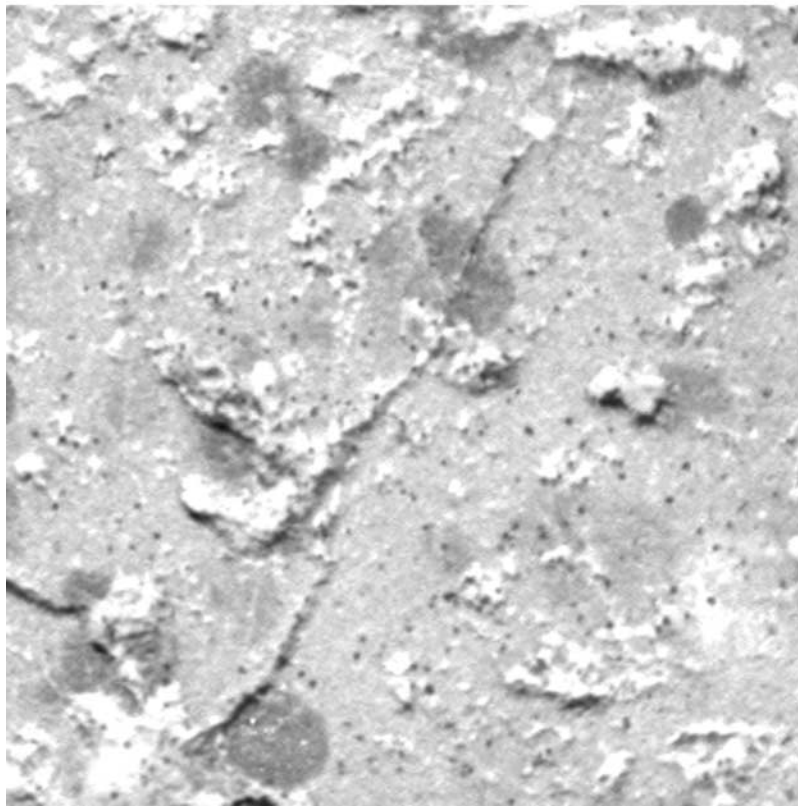


Figure 6. MI close-up of the “One Scoop” Target (Sol 546), showing a normal hematite spherules, irregular intermediate tone blebs, and numerous 2–5 pixel (60 to 150 μm) dark spots. Spots may be “micro”-spherules as discussed in section 2. Image is 1.28 cm wide and taken from the mosaic identified in Table 3.

iron-rich material, possibly the onset of nucleation in a pervasive growth mode. This type of concentration which results in color variations but does not result in a well-developed concretion can be seen in Utah sandstone examples [e.g., *Busigny and Dauphas*, 2007, Figure 2f].

[14] Additional unusual shapes observed in the latter part of the mission include irregular edges on spherules (Sol 727, at Erebus, Figure 8a), a “berry eating a berry” and a “duck-bill” structure (Sol 924, near Victoria) shown in Figure 8b. Again, these shapes are quite rare. Aspherical, irregular textures are more common near Victoria, occurring in the background of MI images of cobble or rock targets on Sols 1103, 1166 and 1168 (Figures 8c and 8d). Another “duck-bill” shaped spherule appears in an MI from Sol 39, and both examples appear to be doublets with one spherule partially broken away. In addition to the prevalence of small, irregular forms, the larger spherules in Figure 8b are obviously oblate with more conical upper surfaces. The small irregular shapes likely represent fused spherules or multiples, formed when two or more originally independent concretions grow into each other. Small spherules are more abundant than large ones, implying more nucleation events such that more doublets and multiples can be expected in samples where spherules are small and numerous. The “berry eating a berry” example may also be explained in this way.

[15] Although they vary in size, Meridiani spherules are mostly spheroidal or oblately spheroidal, with more com-

plicated shapes appearing to be the result of two or more concretions that coalesced during growth. Subtle latitudinal ridge or furrows have been observed on a number of spherules; where the spherules are observed within outcrop, these surficial markings parallel bedding lamination, or reflect the positions of adjacent crystal molds [*McLennan et al.*, 2005]. Such sizes, shapes, and spatial distributions are well known from terrestrial concretions [e.g., *Chan et al.*, 2005; *McBride and Milliken*, 2006; *Margolis and Burns*, 1976]. Spheroidal morphology generally reflects uniform growth in all directions from a point of nucleation, facilitated by a homogeneous host sediment and nondirectional fluid flow. However, at least at the “One Scoop” target there is possible evidence for short-lived pervasive growth as described above.

4. Spatial Distribution and Hematite Indices Using Pancam and Mini-TES Data

[16] The spherules are spatially ubiquitous in plains soils and exhibit a quasi-regular distribution within outcrop rocks [*McLennan et al.*, 2005]. The distribution does vary within and among outcrop facies. In particular, one bed in Erebus Crater at Olympia Outcrop (Sol 630s) had no berries visible at MI imager scale [*Squyres et al.*, 2006a]. In order to survey the spatial distribution in plains soils coordinated remote sensing observations were acquired of the rover near-field between Sols 70 and 1000.

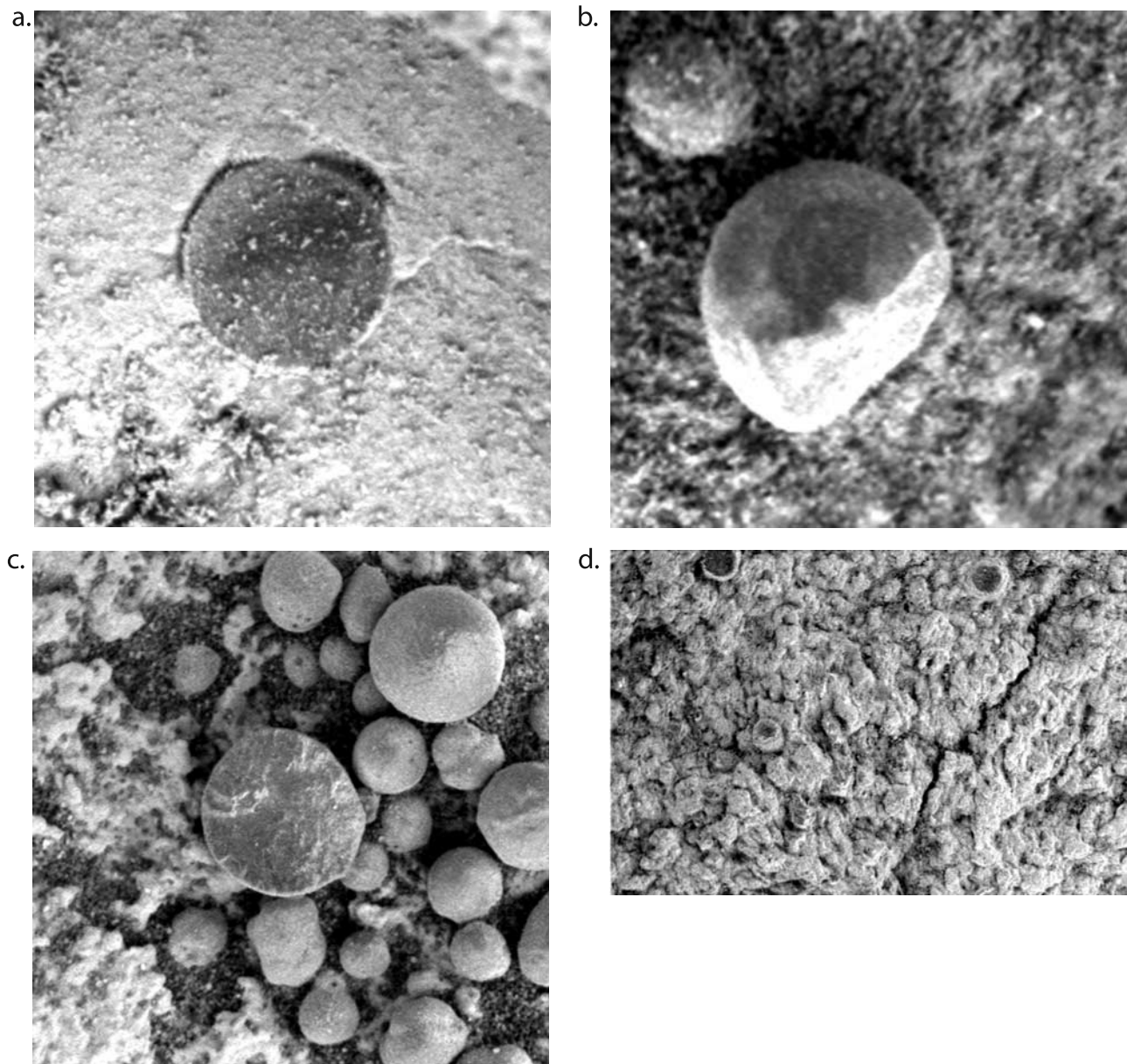


Figure 7. Example of interior of spherules. (a) Possible interior zoning, Sol 139; spherule is ~ 4.8 mm wide. (b) Possible concentric core, Sol 1216; spherule is ~ 3 mm in diameter. (c) Uneven fracture surface, Sol 1166; spherule is 3.6 mm in diameter. (d) Thin coating on small spherules. Sol 962, RAT grind in target Cha; spherule in the upper left is ~ 1 mm in diameter, and image is 1.8 cm wide. Images in Figures 7a and 7d are identified in Table 3. Image in Figure 7b is from 1M236138185FFL85R9P2956M2M2, and image in Figure 7c is from 1M231695945EFF820TP2936M2M1.

4.1. Observations

[17] More than 70 coordinated Pancam and Mini-TES observations were acquired episodically in the traverse from Eagle eastward to Endurance then south toward Victoria Crater. Depending on the data volume and observation time constraints, the “Systematic Foreground” observations were acquired with either a full set (11 unique wavelengths) or a subset of the Pancam geology filters [Bell *et al.*, 2003], and with Mini-TES observations varying from small rasters to longer single-point stares [Christensen *et al.*, 2004]. These observations were made at an elevation angle of ~ 45 degrees, or typically 170 cm directly in front of the

rover. These low-elevation Mini-TES observations allow comparison of distant emission variations with local-scale changes in soil signatures and comparison of optical and infrared hematite spectral features. An initial set of ~ 40 coordinated Pancam observations were identified for detailed analysis that had either full 11-color coverage from 434 to 1009 nm or at least good near-infrared (750 to 1009 nm) coverage to allow optimal discrimination of spherules from soils [e.g., Bell *et al.*, 2004; Soderblom *et al.*, 2004; Weitz *et al.*, 2006; Farrand *et al.*, 2007]. Of the 70 Mini-TES observations, 10 were eliminated because of ringing in the spectra or low temperatures that lead to inverted mirror dust

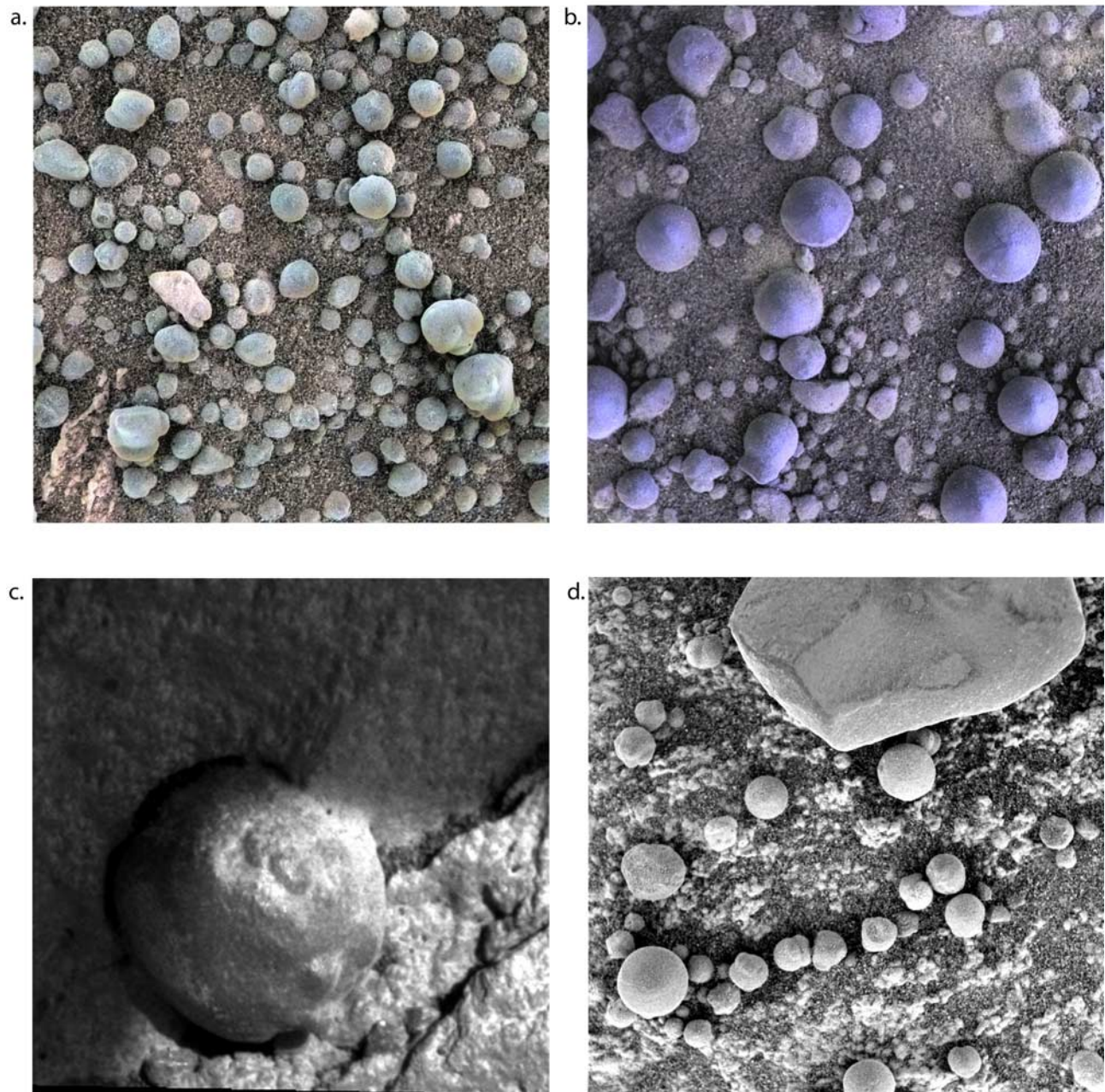


Figure 8. (a) Irregular edges and shapes in spherule material at Erebus/Roosevelt “Panama Canal.” Color composite of MI with Pancam shows that outcrop material is pink, and spherule (hematite) material is blue. The irregular shapes are not adhering outcrop. Pancam color uses left-eye filters L256 in the RGB channels, respectively, from sequence ID P2532 on Sol 729. MI frame is from Sol 727, 1M192737103EFF64LOP2956M2M1. Full MI frame is 3.1 cm wide. (b) Odd shapes “berry eating a berry” top, center, and “duck-bill” bottom and an additional, rare double, upper right, near Victoria. “Duck-bill” is likely a broken doublet. Color composite of Pancam right-eye filters R271 in the RGB channels from sequence ID P2376 on Sol 929 merged with MI image 1M210211203EFF758ZP2936M2M1 from Sol 924. Full MI frame is 3.1 cm wide. (c) Surface irregularities on a large spherule in Cercedilla (Sol 1178), pre-RAT. The small warts on the lower right are about the size of the smallest spherules seen in RAT holes and may be an intact example of the “berry eating a berry” seen in Figure 8b. Spherule is >6 mm in diameter, and image is from the pre-RAT mosaic ID 1MMB78ILF82PER##P2950M222M3. (d) Irregular and fused grains next to “Donut” Sol 1103, MI image 1M226103850EFF798DP2976M2M1, outside Victoria Crater. Similar forms are also seen on Sol 1166 and 1168. Full MI frame is 3.1 cm wide.

Table 4. Mini-TES and Pancam Systematic Foreground Observations Used^a

Mini-TES										Pancam									
Sol	Mtes Seq ID	Spec Notes	Dust-Corrected		Not Hematite Index	Dust Index	Temp	Pcam Seq	Filters	Notes	Scene Description	Ratio RGB	DCS	Percent Error		Best Est	Method	Supervised Classification	
			Band Depth	Hematite Index										Shadow	Est				
70	3715		0.033722	0.0208465	0.0208465	0.01696	287	2584	2		B's scattered on soil, single dune through middle with smaller B's, dense clump on left, red soils ^c		38	6	37	Right (7ch)	13.1		
70	3715		0.031308	0.0221967	0.0221967	0.01268	281	2585 ^b	13										
70	3715		0.034981	0.023718	0.023718	0.00444	259	2585	13	Shadow					20	kmean, right BD			
71	3715		0.03077	0.0211002	0.0211002	0.01531	283	2586	5		scattered B's with few dunes with small B's, density variation, red soils ^e			34	left (4ch)				
81	3715	average not accurate, only three good spectra	0.01232	0.0060401	0.0060401	0.01318	267	2594	2										
82	3715		0.035578	0.0230349	0.0230349	0.02383	278	2596	2										
82	3715		0.03348	0.0216281	0.0216281	0.01642	287	2597	2										
82	3715		0.0358	0.0222567	0.0222567	0.01557	273												
83	3715		0.035592	0.0211949	0.0211949	0.01618	277	2599	2										
83	3715		0.035247	0.0225939	0.0225939	0.00479	259												
88	3715		0.029381	0.0182391	0.0182391	0.02281	283	2545	2										
91	3715	CO2 inverted, hematite is not	0.031633	0.0217249	0.0217249	-0.0129	238	2436	10										
91								2551	12	trench									
92	3715		0.024465	0.0278329	0.0278329	0.00358	261	2550	2										
93	3715	CO2 inverted, hematite is not	0.025601	0.0200837	0.0200837	-0.02888	234	2553	8		very scattered B's, red soils ^d				32	right (4ch)			
94	3715		0.039341	0.0312507	0.0312507	0.02287	275	2555	13	some outcrop	scattered b's on soil and outcrop, bluer soils, minor dense clumps ^f		28	7	32	ratio			
102	3715		0.029367	0.0233364	0.0233364	0.01435	266	2575	5		uniform scattered b's, red soils ^d				32	left (4ch)			
103	3716		0.022388	0.0209246	0.0209246	0.02145	278												
108	3715	CO2 inverted, hematite is not	0.016171	0.0113145	0.0113145	-0.02242	234	2582	13	Shadow + large rock	scattered b's, shadow, light blue b's, very light soils, slight density variation	check			28	ratio			
110	3715	BAD: ringing	0.025601	-0.0638602	-0.0638602	0.02759	264	2460	13	incorrect overlay									
111	3715	CO2 inverted, hematite is not	0.029117	0.0233872	0.0233872	-0.00293	248	2587	13	trench, outcrop and larger cobbles	scattered B's on outcrop and soils, tire trench, 13 large cobbles, bluer soils				28	ratio			
324	3715		0.036058	0.0200856	0.0200856	0.05712	281	2460	13	incorrect overlay									
325	3715	inverted, cold T	0.020324	0.0193461	0.0193461	-0.0758	231												

Table 4. (continued)

Mini-TES										Pancam									
Sol	Mtes Seq ID	Spec Notes	Dust-Corrected		Dust- Corrected, Hematite Index	Dust Index	Temp	Pcam Seq	Filters	Notes	Scene Description	Ratio		Percent Error			Best Est	Method	Supervised Classification
			Band Depth	Hematite Index								RGB	DCS	Shadow	7	29			
359	3715		0.03576	0.0195318	0.08878	288	2530 ^b	13			scattered b's, dune with smaller b's, small density variation, red soils ^c	26	33	7	29	ratio		26.8	
361	3715		0.038894	0.0234446	0.08608	286	2545 ^b	13			scattered b's, dune with smaller b's, higher density below dune, red soils ^c	27	25	5	41	ratio		26.9	
363	3715		0.044627	0.0288105	0.09571	289	2451	7			scattered b's, small density variation, unknown soil				40	ratio			
365	3715		0.04172	0.0274119	0.08305	289	2451	7			dune with small b's, dense b's, unknown soil				46	ratio			
382	3715		0.039364	0.0242828	0.10538	295	2558 ^b	13			scattered b's, few small cobbles, red soils ^d	27	27	7	36	Right (7ch)		22.0	
395	3715	average ok, one w/ringing	0.034775	0.0211858	0.09875	296	2558 ^b	13			dune with small b's, more dense b's below dune, red soils ^c	34	35	8	39	BD		13.3	
518	3715		0.031544	0.0154419	0.12876	292	2563 ^b	13			dune clumps of b's with some small cobbles, red soils ^d	37	31	7	38	Right (7ch)		18.9	
522	3715		0.023169	0.0115659	0.0592	274	2456 ^b	13			small dune variation of b's, uniform size, very red soils ^d	26	31	12	40	Right (7ch)		15.6	
527	3715		0.036744	0.0160104	0.14582	293	2456 ^b	13	sol 528		scattered b's with few small dunes in corner, some small cobbles, very red soils ^d	28	30	9	36	Right (7ch)		26.6	
529	3715		0.039924	0.0199753	0.14774	294	2456 ^b	13	sol 530		scattered b's with some cobbles, very red soils ^d	30	24	9	36	Right (7ch)		25.0	
531	3715		0.035243	0.0149035	0.15039	294	2456 ^b	13	sol 532		scattered b's with lots of small cobbles, density gradient to right, very red soils ^d	25	29	8	35	Right (7ch)		35.7	
534	3715		0.03541	0.0166934	0.15214	292					scattered b's with small cobbles, very red soils ^d	21	30	5	35	Right (7ch)			
535	3715	ringing average is bad					2569	13	possibly 534, with 535 on 536		lots of dune features, smaller b's and larger b's, red soils ^e								
537	3715	average BAD: ringing					2444	6	sol 538		dunes with greater density, same size b's, red soils ^e		51		60	left (3ch)			
537							2444	6	sol 538		lots of dune features, smaller b's and larger b's, red soils, looks exactly like sol 537_1 ^e								
540	3715	average OK, but one w/ringing	0.033395		0.14316	296	2447	3	sol 541				66		38	left (3ch)			

Table 4. (continued)

Mini-TES										Pancam								
Mtes Sol Seq ID	Spec Notes	Dust-Corrected		Not Dust-Corrected, Hematite		Dust Index	Temp	Pcam Seq	Filters	Notes	Scene Description	Ratio		Percent Error		Best Est	Method	Supervised Classification
		Band Depth		Index								RGB	DCS	Shadow				
540 3715								2447	3	sol 541	dune features (like previous) but only in corner, scattered b's with declining density to right, red soils ^e scattered small b's with many small to larger cobbles and some small outcrop, red soils ^g some b's on outcrop, scattered on soils, some small cobbles, bluer soils ^f B's scattered on soil, mostly shadow, red soils, light berries very light soil and b's, small b's in dune features, shadow B's scattered on soil, small density variation, red soils ^d lots of outcrop, B's thick on soil between them, small tire track, some small cobbles, bluer soils ^f B's scattered on light red soils ^d B's scattered on soil, small density variation, red soils ^d small B's clumped in dune like lines, red soils ^e lots of outcrop, B's on soil between them, few cobbles, some b's on outcrop, bluer soils ^f	25	32	7	34	Right (7ch)	36 left (3ch)	
550 3715		0.021248		0.0154905	-0.00679	265	2579	13	some with larger rocks									
559 3715	highly variable	0.02589		0.0127562	0.1026	277	2586	13	outcrop				24	35	5	32	ratio	
570 3715	inverted, cold T					255	2515	13	small frame, mostly shadow. Sol 571 shadow							24	ratio	
577 3738		0.020621		0.0061985	0.15931	297	2456	13								39	Right (7ch)	
579 3738		0.033933		0.0171161	0.15042	291	2456	13					33	31	10	37	Right (7ch)	
581 3738	highly variable	0.026424		0.0141546	0.13896	281	2456	13	outcrop				30	41	7	26	Right (7ch)	
584 3715		0.026273		0.0202903	0.02152	277	2542 ^b	13								38	Right (7ch)	16.8
602 3738		0.03867		0.0186837	0.20714	290	2586 ^b	13					39	38	10	41	Right (7ch)	32.2
604 3738		0.024428		0.008516	0.18013	298	2534 ^b	13								37	Right (7ch)	17.5
609 3715	Highly variable	0.018465		0.0085987	0.0989	274	2537	13	outcrop				20	26	3	33	Right (7ch)	

Table 4. (continued)

Mini-TES										Pancam						
Sol	Mtes Seq ID	Spec Notes	Dust-Corrected		Not Hematite Index	Dust Index	Temp	Pcam Seq	Filters	Notes	Scene Description	Ratio RGB	Percent Error			Supervised Classification
			Band Depth	Dust-Corrected, Hematite Index									DCS	Shadow	Best Est	
752	3480	very strong dust contribution	0.02366	0.0021077		0.22751	274	2548	13	outcrop	B's on outcrop, lots of smaller B's/soil, not a good percent, lots of small cobbles, possibly bluer soils (only right filter) ^f	34	38	6	16	right (7ch) (not good)
754	3480	"	0.020082	-0.0029288		0.27546	277	2550	13	wheel track	small light B's on light red soil, tire track through middle, lots of small cobbles	22	25	1	14	BD
761	3715		0.029889	0.0037931		0.26935	276	2552 ^b	13		B's scattered on light red soil ^d	33	34	10	23	Right (7ch)
772	3485	"	0.0362	0.0053579		0.25662	284	2456 ^b	13		B's on soil, density variation due to minor dune clumping ^d	33	44	7	39	Right (7ch)
779	3715	"	0.027803	0.00168		0.26275	274	2456	13	very few larger rocks	scattered dune clumped B's, uniform size, lots of small cobbles, very red soils ^g	21	33	10	32	Right (7ch)
786	3740	has hematite band	0.017529	0.0162515		0.01992	250	2658	13		B's scattered on soil, lots of small cobbles, red soils ^d	32	35	8	20	Right (7ch)
793	3740	very strong dust	0.037466	0.003841		0.26654	272	2461	13		B's clumped in dune like lines ^c	46	40	12	42	Right (7ch)
795	3740	inverted, cold T					227	2577	13		small, very scattered B's on very red soil ^d	28	32	7	21	Right (7ch)
797	3740	inverted, cold T					225	2578	13							
801	3740	has hematite band	0.014246	0.0122447		-0.01615	249	2583	7	sol 802, R7 not good, unsure if correct						
808	3740	inverted, cold T					238									
815	3740	has hematite band	0.012728	0.0104153		0.02696	247	2593 ^b	13		small B's clumped in dune like lines, red soils. ^c					34.6
832	3740	inverted, cold T					242									
844	3740						242									
864	3740	inverted, cold T	0.014666	0.0118337		0.0221	242 230			R6 not good						

Table 4. (continued)

Mini-TES										Pancam							
Sol	Mtes Seq ID	Spec Notes	Dust-Corrected			Dust Index	Temp	Pcam Seq	Filters	Notes	Scene Description	Ratio RGB	Percent Error		Best Est	Method	Supervised Classification
			Band Depth	Not Corrected	Dust-Corrected, Hematite Index								DCS	Shadow			
874	3740		0.018547		0.002849	0.24001	271	2546 ^b	13		small B's clumped in dune like forms, more dense B's on right side of image ^c B's scattered on soil, lots of small to large cobbles ^g B's scattered on soil, few small cobbles ^d						37.8
884	3743		0.025408		0.0065842	0.20607	264	2461 ^b	13								22.6
913	3715		0.037369		0.0050055	0.24576	269	2570 ^b	7								29.4
917	3740	inverted, cold T					239										
942	3715		0.026313		0.0047884	0.2657	270			Not found							
960	3743		0.010511		0.0022176	0.18569	257			Not found							
994	3715	inverted, cold T					240										
999	3715	inverted, cold T					250										

^aFootnotes in Pancam descriptions are used to identify similar scene content. DCS is decorrelation stretch.

^bObservations used in final comparison between Mini-TES and Pancam using supervised classification.

^cRight-eye filters only.

^dRipple forms.

^eLeft-eye filters only.

^fImages that contain significant outcrop. Some Pancam images were acquired on the morning following the Mini-TES to optimize illumination. Derivation of hematite indices is described in section 4.

^gRipple forms but with more cobbles.

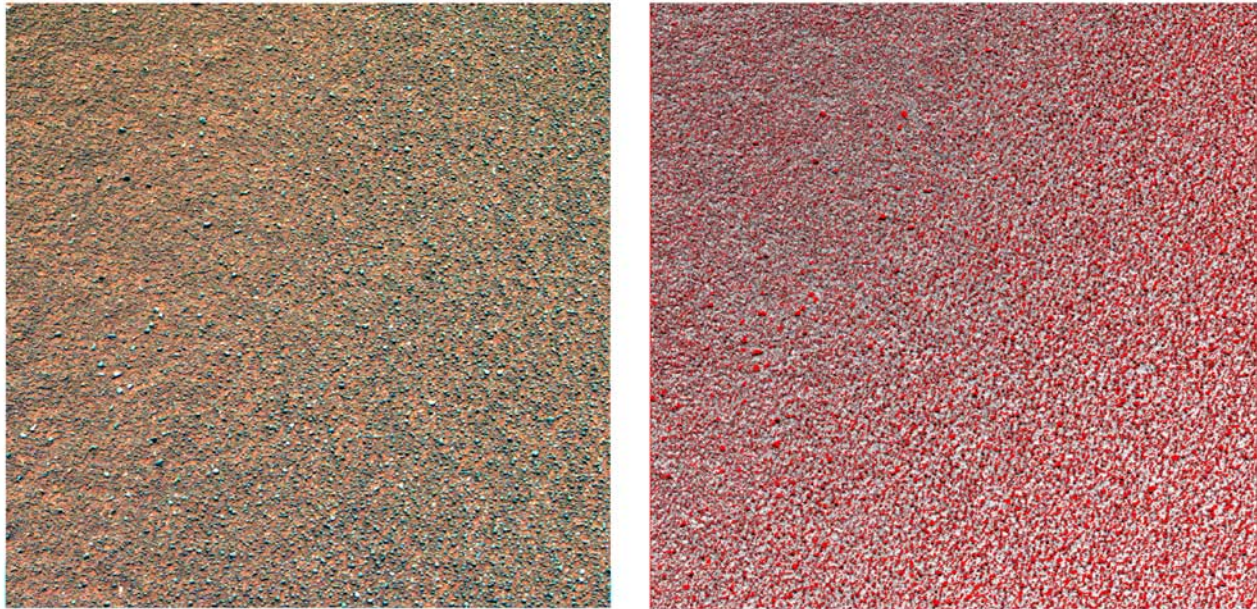


Figure 9. (left) False color composite of a typical Pancam Systematic Foreground image (Sol 532 sequence P2456) created from L2 (753 nm), L5 (535 nm), and L7 (432 nm) filters. (right) Fractional area coverage by hematite using the ratio method. Areas classified as hematite are red, and this scene is 29% coarse hematite coverage.

contributions. These observations are summarized in Table 4. Preliminary unsupervised K-Means classification of Pancam data was complicated by heterogeneous surface cover, usually outcrop or large cobbles, and resulted in large uncertainties in scene classification, as described in section 4.2. Therefore, we further reduced the complementary data set to 19 observations that had both Pancam and high-quality Mini-TES spectra of homogeneous soils (Table 4 and Figure 9). We determined a hematite cover or band strength index using the band depth of the infrared absorptions from Mini-TES spectra and a color ratio index and supervised classification scheme from Pancam data.

4.2. Pancam Methods

[18] In order to best estimate the fractional area covered by “blueberries” we explored a number of classification schemes. These included unsupervised classification of either left-eye or right-eye filters, band ratios, relative band depths and band slopes as shown by *Farrand et al.* [2007] to be useful for discriminating spherules against the background soil. In all cases we used calibrated radiance factor I/F data [Bell *et al.*, 2006] and K-Means or Minimum Distance classification algorithms available through ENVI[®] image processing software. Images were exported as either left- or right-eye image cubes from Pancam display tools into ENVI. As noted by *Farrand et al.* [2007] Pancam right-eye filters do a better job of classifying spherules against the soil, as they capitalize on the 900 nm absorption feature and the pronounced increase in reflectance from the 934 to the 1009 nm band that is associated with the gray hematite in the spherules. The methods that visually classified the majority of spherules with only small misclassifications of nonspherule soils using unsupervised techniques, were either a

decorrelation stretch (DCS) of right-eye filters or a thresholded band ratio.

[19] The first method performs a DCS using right-eye filters R3,2,1 (803 nm, 764 nm, and 436 nm, respectively). The blue channel of the DCS image is then ratioed to the ratio of two other Pancam filters, R6/R7 (934/1009 nm). This method uses both the slope increase and low blue albedo of the spherules. A threshold in the ratio that separates spherules from soil is selected. The scene area covered by all pixels above the threshold is then determined. The second method uses the R1/R2 ratio in a simple color composite (Red-Green-Blue) with R1 (G) and R6/R7 (B). As identified by *Farrand et al.* [2007] these ratios enhance the near-infrared absorption band associated with the spherules and provide spectral contrast against basaltic sands, cobbles or other non-“bulk” hematite soil materials [e.g., *Weitz et al.*, 2006]. This color composite was then used in a K-Means unsupervised classification to determine area covered by spherule material.

[20] In spite of the method refinement, fairly large uncertainties exist in defining image thresholds or in areas classified as spherules. Shadowing at the edge of spherules, illumination gradation across the scene, misclassification of dust covered spherules as soil, and irregular particle density associated with aeolian ripples in the scene all contribute to misclassification or errors in calculations of area covered by spherules. Estimates of the areas misclassified as spherule that were not, or dust covered spherules not classified as such, range from 5 to 12% of the total scene area. Variations among the unsupervised methods were as large as 15% in total area estimated to be covered by spherules. Early, unsupervised methods also misclassified basaltic cobbles as spherules and led us to a supervised method where image

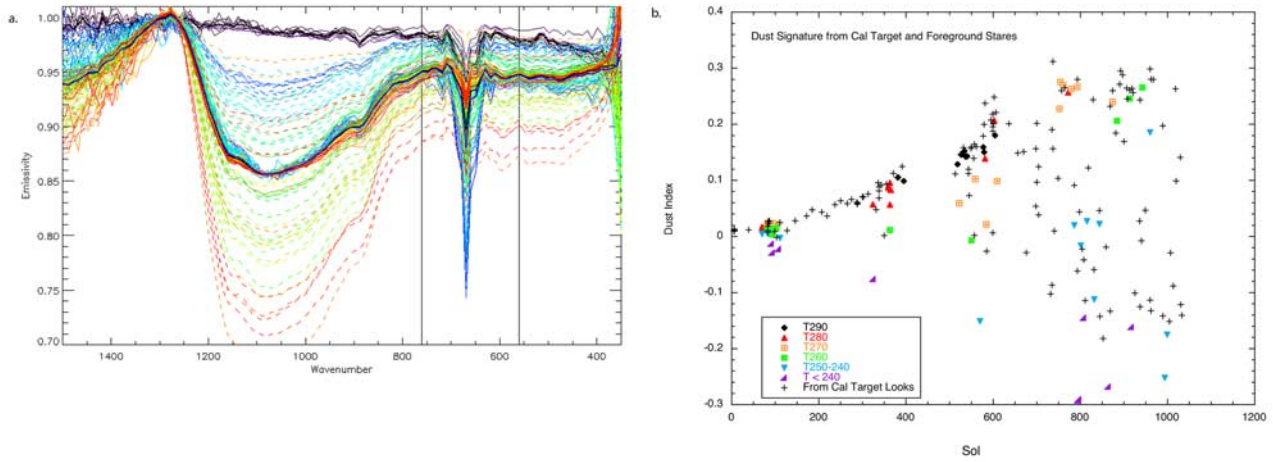


Figure 10. (a) Mini-Thermal Emission Spectrometer (Mini-TES) emissivity spectra of the external calibration target showing increasing contribution from both dust on the target and internal dust signature on the instrument mirror (dotted lines). Spectra scaled to the same value (solid lines) and the average (black line) used to correct for the dust contribution to soil observations are also shown. Note appearance of the envelope below 550 cm^{-1} , on the right hand side, that will interfere with hematite band strength determinations when the dust contribution is high. (b) Increase in Mini-TES mirror dust contribution over the course of the mission. The “Dust Index” is determined from foreground soil observations grouped by target temperature. A second collection (plusses) was determined from the calibration target stares. Depending on the relative temperature of the target and instrument, the dust signature is either seen in absorption (positive index) or emission (negative index). Dust index is increasing over time, regardless of target temperature. Later in the mission an “ideal” temperature difference (ΔT) between target and instrument can largely eliminate the appearance of the dust signature, though in practice very few surface observations were acquired with these optimal conditions.

end-members are selected from the first, DCS method. Small training areas of spherules, soil and shadow were used in a Minimum Distance supervised classification on all right-eye filters to determine fractional scene areas for the remainder of the image. Figure 9 shows an original RGB Pancam scene and its final classified hematite coverage for typical homogeneous areas where the method worked well; that is, misclassified or unclassified spherule edges were estimated to be $<10\%$ of the total scene area.

4.3. Mini-TES Methods

[21] The simplest method to determine a hematite “index” is based on calibrated emissivity spectra. The index is calculated from sum of the two absorption band depths relative to the peak height, $(A - B) + (A - C)$, where A is the emissivity at the peak (500 cm^{-1}) and B and C are the values of the band centers at 550 cm^{-1} and 450 cm^{-1} , respectively. Complicating this approach, however, is that over the course of the mission, dust has accumulated on the Mini-TES pointing mirror. This creates a large, broad feature in calibrated emissivity spectra (Figure 10a). For much of the mission, this signature has not impacted the lower wave numbers (longer wavelengths) where the hematite features occur. However, this dust contribution has increased over time, such that in later Sols a very strong dust signature will also affect the hematite wavelengths (Figure 10a). *Smith et al.* [2006] have noted that the character of dust on the mirror is different between Spirit and Opportunity showing a slow but continuous increase on Opportunity. We have observed similar trends in both the

external calibration target and soil observations. We have determined a “dust index,” that is the difference between the emissivity of the continuum near 1275 cm^{-1} and the maximum feature strength near 1100 cm^{-1} . This dust index is shown versus Sol number in Figure 10b. To correct for this artifact and more accurately determine the hematite abundance we have developed a method to correct for the spectral shape of the dust contamination.

[22] Depending on the relative temperature of the target and instrument, the dust signature is either an absorption or emission feature. Our correction uses only observations in which the dust is an absorption feature (i.e., the surface target is warmer than the instrument and mirror). We then use an average “dust” signature determined from observations of the external calibration target after Sol 300 when the signature became prominent (Figure 10a). This average dust spectrum was scaled at wave numbers near 1100 cm^{-1} to the size of the dust feature in the surface observation. The scene and scaled average dust spectra were then ratioed to effectively remove the dust signature. A “dust-corrected” hematite band depth is then determined by taking the difference between the emissivity value of the shoulder at 750 cm^{-1} and the depth of the hematite feature at 550 cm^{-1} (shown by horizontal bars in Figure 11b).

[23] Both the simple band index and the dust-corrected band depth correlate extremely well, although the band index is consistently a smaller value than the dust-corrected band depth. We prefer the dust-corrected band depth in most instances, except when the dust signature is very low, early in the mission. Figure 11 shows the correlation

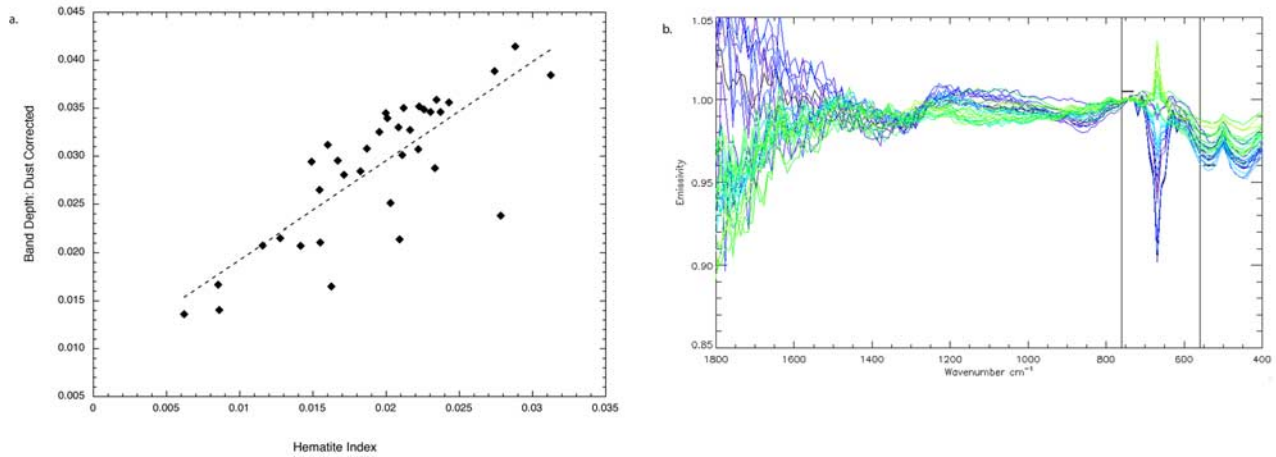


Figure 11. (a) Correlation between the Mini-TES dust-corrected band depth and the uncorrected hematite “band index”; dotted line is the best fit. The dust-corrected band depth is preferred, particularly for later Sols. (b) Dust-corrected Mini-TES spectra of systematic soil observations. Hematite band depth is determined using the band shoulder and band center shown as horizontal black bars as described in section 4.3. Vertical black lines note the region that has interference from atmospheric CO₂ absorption between 730 and 600 cm⁻¹.

between the two methods and the final dust-corrected spectra. Dust-corrected spectra are very similar to plains scans acquired before Sol 80 when there was not a significant mirror dust contribution to the observations (see, e.g., section 5, Figure 13).

4.4. Correlation of Pancam and Mini-TES Indices

[24] Using a limited set of Pancam images where the supervised classification schemes work well, there is rough correlation between the dust-corrected Mini-TES hematite

band depth and the Pancam fractional area covered by spherules suggesting that these two methods are seeing similar components of the soils (Figure 12a). That is, both the Pancam near-infrared absorption and the strength of the midinfrared hematite features correlate with the abundance of spherules on the soil. Scatter in the plot may be accounted for by differences in the field of view of the Pancam subframes and Mini-TES spot or raster sizes, as well as by fairly large classification uncertainties noted previously. Mini-TES observations of outcrop that is slightly

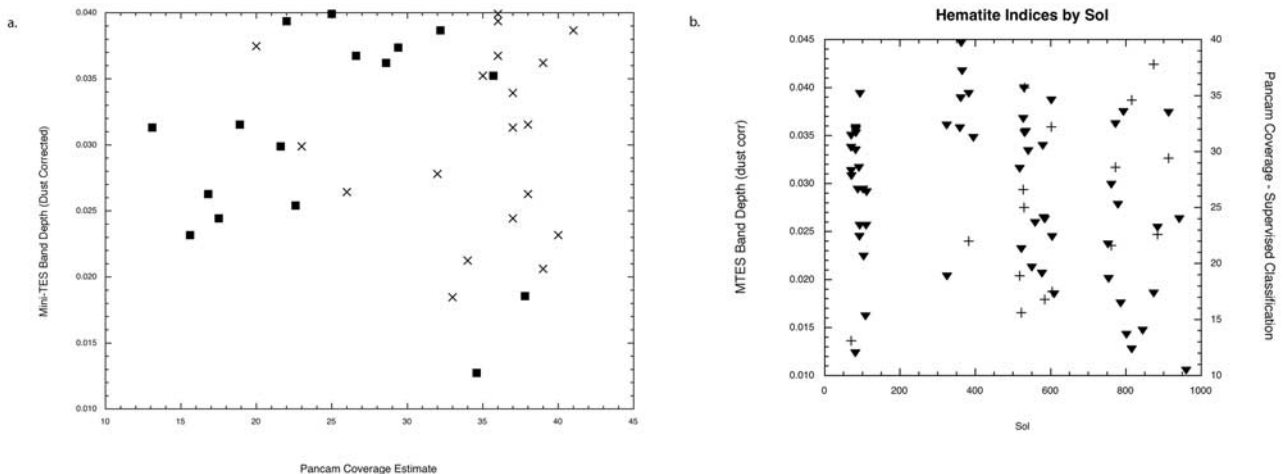


Figure 12. (a) Derived Pancam spherule area cover versus Mini-TES hematite band depth (dust corrected). The “X” values are a best estimate using right-eye band thresholds as described in section 4.2. Methods were revised on the basis of the lack of correlation. The solid squares compare the final supervised classification method to Mini-TES of homogenous soils. Except for two outlier points at high Pancam coverage, the area covered and Mini-TES band depth show a reasonable positive correlation. (b) Pancam and Mini-TES hematite indices by Sol. The inverted triangles show Mini-TES dust-corrected band depth, and the pluses show Pancam derived area covered by spherules. Mini-TES uses all possible Sols, regardless of surface cover. Pancam shows only homogenous soils. See also Table 4.

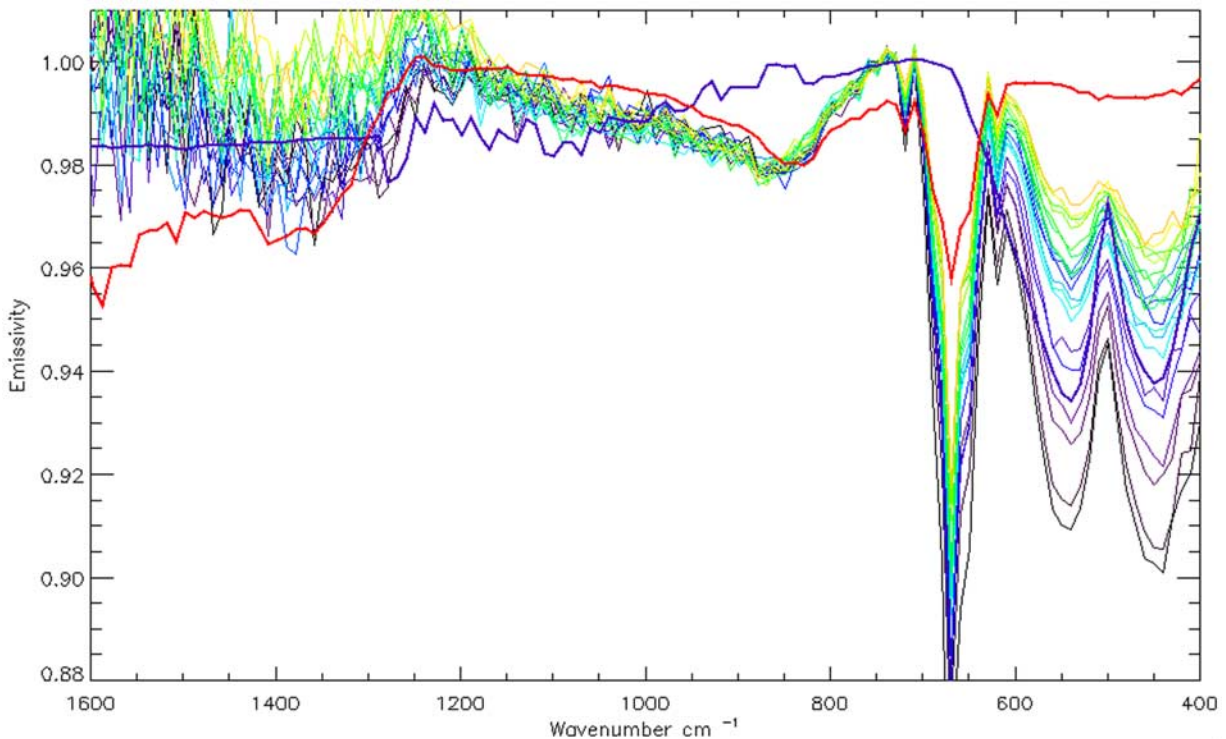


Figure 13. Increase in hematite band strength with distance on the plains. This observation, 1T134582706EMR0932P3282N0A1.QUB, acquired on Sol 72, is 65, 2 “ICK” measurements that have been average in groups of three to improve signal to noise as described in section 5. Color varies from high elevation (black is farther away and deeper bands) to low elevation (yellow is near-field and weaker bands). Data have been scaled to a consistent emissivity value near 750 cm^{-1} . The thick purple line is the library spectrum of hematite, and the thick red line is a typical surface dust spectral signature from the Spirit Mini-TES.

darker in Pancam multispectral images (purple in composite L357 decorrelation stretch (DCS) images corresponding to the “LFS” spectral class of *Farrand et al.* [2007]) show a stronger hematite signature. This may suggest that Mini-TES and Pancam are sensing very near surface components of alteration rinds, though chemical differences in APXS, particularly enhancement of Fe, are weak [*Knoll et al.*, 2008].

4.5. Spatial Distribution of Hematite Indices

[25] The systematic foreground observations were typically acquired every week or 10 Sols, especially during drive segments on the long traverse south to Victoria Crater. As such, the observations only acquire whatever was randomly in front of the rover and there is significant scene variability. This diversity makes it difficult to explore trends over the traverse from Eagle to Victoria, but in general no strong changes in hematite index are observed (Figure 12b). There is large Sol to Sol variability, as expected from soil, outcrop and ripple diversity seen in the Pancam images. Using the supervised classification method and homogeneous soils, scene area covered by spherules in Pancam ranges from roughly 10 to 40% (Figure 12b). The Mini-TES hematite band depth varies from 0.01 to 0.045. This spatial coverage is consistent with large area averages estimated by MGS-TES of 10% hematite and roughly 50% basaltic material [*Christensen et al.*, 2000]. Neither Pancam

nor Mini-TES measures of hematite abundance show any systematic trend that would correlate with the decreasing spherule size observed with MI. That is, regardless of spherule size, the hematite abundance in the soil lag depends more on local variability rather than on regional trends.

5. Directional Emissivity Effects

[26] Mini-TES plains scans were obtained inside Eagle Crater, where Opportunity was below the local plains level, just outside of Eagle Crater, and south of Endurance in the vicinity of the heat shield. A series of ripple slope observations were also made at Purgatory, the ripple in which Opportunity temporarily got stuck in June 2005. We analyzed the plains scans from outside Eagle Crater (Sols 57–72), and in the vicinity of the heat shield (Sols 354–372). In both cases the rover was on fairly level terrain so that the instrument elevation angle can be used to determine an approximate surface emission angle through simple geometry. The data cover a wide range of azimuths and generally observe from near the rover to the horizon over homogenous terrain.

[27] The vertical scan obtained just outside of Eagle Crater shows that there is a strong and consistent pattern of increasing band strength with larger emission angles (smaller instrument elevation angle) on the plains (Figure 13). This

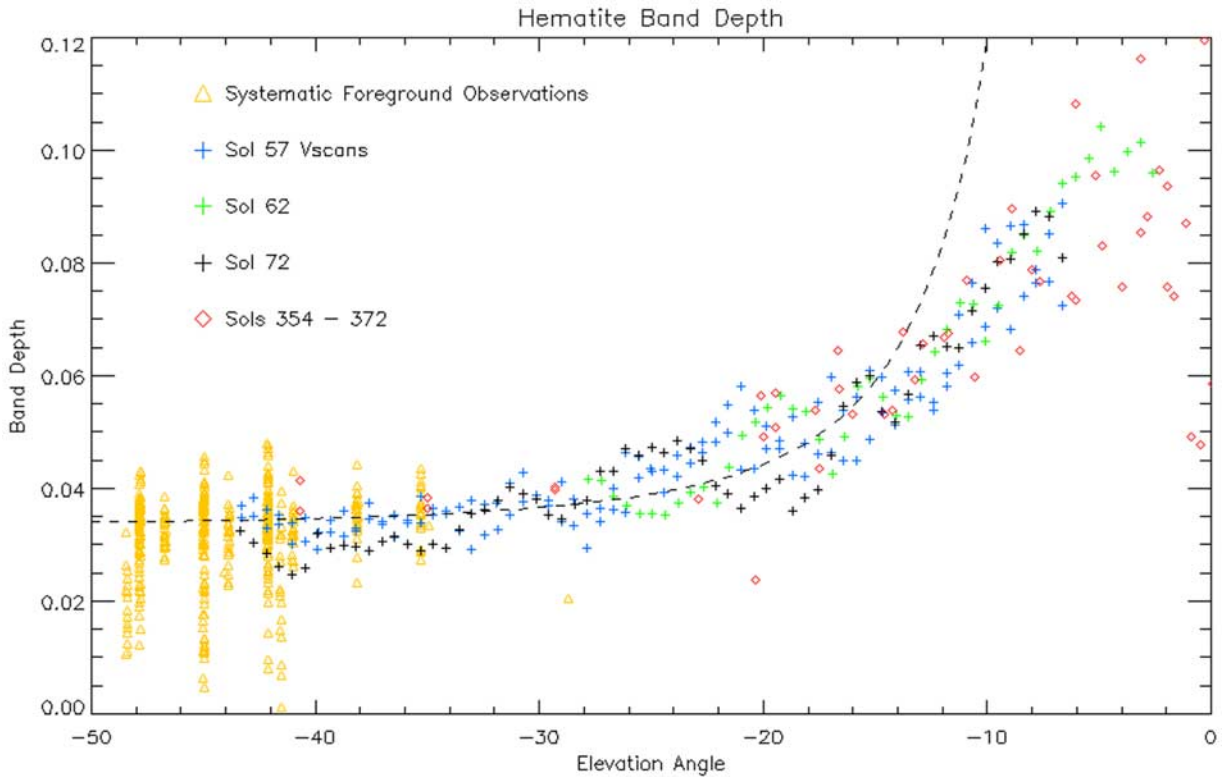


Figure 14. Hematite band depth with elevation angle or directional increase in band strength with increased emission angle. The predicted curve as a function of projected area is shown as the dotted line. Possible reasons for the deviation above -15° degrees elevation are discussed in section 5. Variability in the systematic foreground observations is due to scene components as described in section 4.

observation, P3282, was acquired on Sol 72, before the mirror dust became a significant factor. The observation is 65 spatial positions each of which is a sum of two individual spectral measurements (identified by the Incremental Counter Keeper or number of “ICKs”), at varying elevation angles. In order to improve the signal to noise, these 65 have been grouped into 20 averages of 3 of adjacent elevation angles. It should be noted that while the hematite features are observed to increase significantly, there is no associated increase in band strength in the $10\text{-}\mu\text{m}$ region, where the shape is similar to that of dusty surfaces at Spirit’s landing site [Ruff *et al.*, 2006]. If Mini-TES were also sensing a silicate component within the spherules we would expect to also see an increase in band strength at $10\text{ }\mu\text{m}$, similar to the increasing hematite absorptions. The lack of an increase of absorption in the spectral region associated with silicates suggests that hematite is the only mineral detected in the spherules by Mini-TES. This observation is consistent with the spherule mineralogy derived from the MB spectrometer [Morris *et al.*, 2006], although that instrument is only sensitive to iron-bearing minerals.

[28] Figure 14 shows the elevation angle dependence of hematite band strength from observations on different Sols and at separate locations. The increase in projected area of the Mini-TES spot size is predicted to follow a $(1/\cos(q))^3$ curve, where q is the complement of the elevation angle. This approximate fit is shown as the dashed line. Although this measure works well nearest the rover, the observations

deviate from this simple geometrical relationship at elevations above -15° . Small deviations from the projected area fit at any given elevation angle may be accounted for by heterogeneity in spherule cover, variable terrain geometry, noise levels in the early mission, low-sum scans, and the extreme distances involved in the smallest elevation angle observations. The highly variable foreground observations (see section 4.5) also cluster around the trend observed from the vertical scans at the lowest elevation angles.

[29] The lack of an absorption feature at 390 cm^{-1} in the spectra from TES in orbit and Mini-TES on the surface suggests that the emission is dominated by a single crystal axis (c-face) of hematite, as can occur if the crystal grains are oriented (laminated or platy structure) [Lane *et al.*, 2002; Glotch and Bandfield, 2006]. This may occur in either “bulk,” i.e., coarsely crystalline material, or in small, but oriented crystallites [Golden *et al.*, 2008]. In recent work, Glotch *et al.* [2006] modeled spectra from spherules using Fresnel reflectance theory and noted that either random thin plates or interior concentric laminations could account for the observed spectra. Radial needle orientation could also account for the observed spectra, as seen in synthetic spherules created under hydrothermal conditions [Golden *et al.*, 2008]. We note that in all of the Fresnel models band center shifts and relative changes in band strength are observed at emission angles of 75° : the same point at which the directional emissivity variation deviates from a simple geometric curve (Figure 14). Recent work by

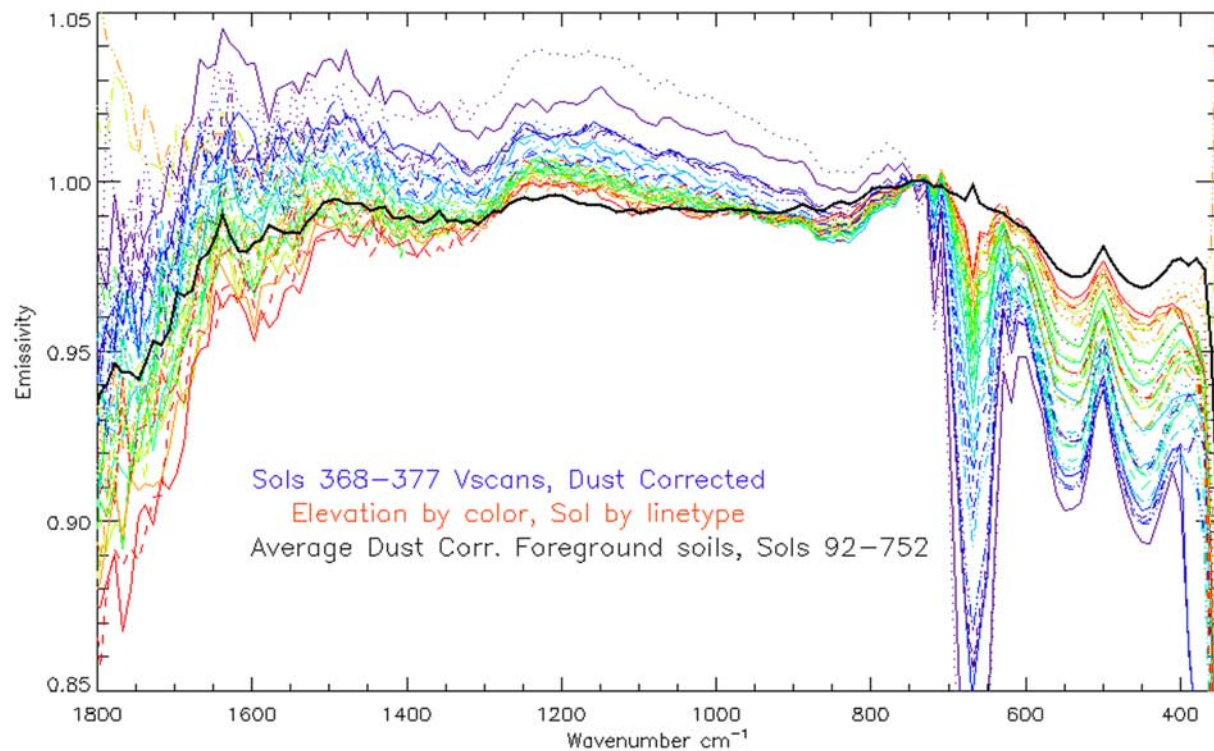


Figure 15. Dust-corrected vertical scans in the vicinity of the heat shield. Higher-elevation (farther distance) again results in an increase in the hematite band strength. These long averages (100 “ICKs”) show the appearance of a bound water feature near 1640 cm^{-1} . The feature is also seen in the average of 20 foreground soil observations, shown as the thick black line.

Pitman et al. [2006] also suggests that emissivity band strength increases at higher emission angles.

6. Other Spectral Features

[30] As described in section 5, vertical Mini-TES scans acquired early in the mission, before the dust contribution became significant, do not show an absorption increase that would be associated with an additional silicate component in the spherules. They only show a component typical of dusty surfaces. Observations of extensive sand patches and ripple forms (e.g., within Eagle, or the target Auk, Sol 221 in Endurance, and the ripple forms in the bottom of Endurance Crater) have noted the general basaltic envelope of soils in addition to the surface dust shape seen in Figure 13 [Christensen et al., 2004; Glotch and Bandfield, 2006; Rogers and Aharonson, 2008]. This broad basalt envelope is also weakly observed in a number of individual outcrop stares and may be attributed to distributed sand on the outcrop [Grotzinger et al., 2005]. Dust-corrected foreground stares also exhibit spectral envelopes between 800 and 1200 cm^{-1} that range between the surface dust “V” feature at 850 cm^{-1} and a broader basaltic shape that spans the spectral range (Figure 11b). Figure 11b also shows that these foreground observations suggest the presence of an additional absorption component at higher wave number (shorter wavelength) than 1200 cm^{-1} . In these foreground observations, this feature appears in corrected spectra that have a basalt-shaped envelope rather than a dust-shaped envelope. This is likely due to better signal to noise in the

dark, warmer sand observations, and suggests that the material causing the high wave number absorption is not tied to the dust end-member, as was derived by Glotch and Bandfield [2006, Figure 5].

[31] In order to explore this component in more detail, vertical scans from near the heat shield were corrected for the “mirror dust” contribution and are shown in Figure 15. In addition, an average of 20 foreground spectra was also calculated in order to improve the signal to noise and is also shown in Figure 15. In the vertical scan data, although the slope varies, the strength of the high wave number absorption does not change with distance or projected area, similar to the unchanging silicate absorption (section 5). These spectra typically show the dusty “V” shape, though some have slightly broader, more basaltic envelopes. In the foreground average, the 800 to 1200 cm^{-1} region is a basaltic envelope but the absorption at high wave numbers is quite clear. All these spectra, regardless of “dust” or “basalt” envelope, show an absorption beginning near 1200 cm^{-1} and extending to 1800 cm^{-1} . The overall absorption in individual spectra is noisy, but is well resolved in the average foreground spectrum. This spectral shape also includes a weak, but discernible peak near 1640 cm^{-1} associated with water of hydration. This shape is consistent with similar envelopes that have been ascribed to minor carbonate [Bandfield et al., 2003] or sulfates [Bishop et al., 2004; Lane et al., 2004] in the surface dust, water in hydrohematite [Golden et al., 2008], and bound water in surface soils at the Spirit landing site [Kuzmin et al., 2006]. It should be noted that in many hydrated particulate sam-

ples, the water is expressed not just as the narrow peak at 1638 cm^{-1} , but as a broad envelope on both sides of this feature [e.g., *Salisbury et al.*, 1991]. This may result from an interplay between the Christiansen frequency, scattering effects, and the water absorption feature, but has not been discussed in the literature. By empirical comparison with laboratory data of a variety of hydrated samples, the entire envelope at high wave numbers may be due to water in nonspecific mineral sites. The band strength of the hydrated component was determined using ratios of several channel averages for the band minimum at 1400 cm^{-1} to the shoulder at 1200 cm^{-1} and also the water peak at 1640 cm^{-1} relative to the minimum at 1400 cm^{-1} and shows no trend with hematite band strength in the vertical scans nor does it correlate with either a dust shape or a basalt shape in the $800\text{ to }1200\text{ cm}^{-1}$ region. Given this lack of association with other major components it seems that this feature represents a soil or other surface component that is locally variable. At least some portion of the feature arises from the relative contribution from surface dust, as this feature occurs in the surface dust end-member spectral shape of *Glotch and Bandfield* [2006]. Other contributions may occur from a weak sulfate component in the soils from eroded outcrop, or water in exchange with the atmosphere and variable with both season and time of day or local soil type [*Kuzmin et al.*, 2006; *Milliken et al.*, 2007].

7. Discussion: Earth Analogs

[32] It is unlikely that any terrestrial site will specifically reflect both the physical and chemical circumstances of Martian deposition and diagenesis [e.g., *Knoll et al.*, 2005; *Fernandez-Remolar et al.*, 2005]. On the surface of Mars, the starting materials are almost exclusively basaltic, and geochemical reactions appear to have been water-limited. The set of terrestrial environments that replicate both these features is small. Nonetheless, specific terrestrial environments can illuminate physical processes or chemical reactions likely to have been important on Mars.

[33] Small rounded particles exist in a wide variety of materials with varying origins on Earth. Diagenetic concretions, impact spherules, and orbicular igneous rocks are all known and well studied. Several specific examples have been explicitly claimed as analogs to Meridiani spherules: small spherules formed by acid vapor or fluid interaction with volcanic tephra [*Morris et al.*, 2005], the diagenetic concretions of southern Utah [*Chan et al.*, 2004], an orbicular carbonatite dike in South Africa [*Haggerty and Fung*, 2006], and accretionary lapilli in impact surge deposits in New Mexico and South Africa [*Knauth et al.*, 2005].

[34] As noted by *McLennan et al.* [2005], the Meridiani structures occur in sedimentary rocks, are spherical or oblatelike spheroidal, are composed dominantly of hematite, have latitudinal ridges or furrows marking their surfaces, sometimes occur as two or more coalesced spheroids, and are distributed three-dimensionally, with interspherule distances more regular than random. Also notable are features not exhibited by Meridiani spherules: they do not occur in concentrations along bedding surfaces within outcrop rocks, and in nearly all cases, they do not show macroscopic evidence of internal structure. In combination, these observations strongly support the interpretation of Meridiani

spherules as concretions that accreted diagenetically in a more or less homogeneous sediment with no strong directional flow of groundwater [*McLennan et al.*, 2005].

[35] Terrestrial concretions exhibit a wide range of mineralogies, although carbonates and silica are most common. Concretions found in the Jurassic Navajo Sandstone in southern Utah, display many of the physical features recorded at Meridiani Planum, although they display a wider range of morphologies, are concentrically zoned, tend to be larger than the Martian examples, and contain limited iron oxide minerals [*Chan et al.*, 2004, 2005]. Iron concentrations are high only in the rims of these nodules, having precipitated as cements, the centers being dominated by silica [*Busigny and Dauphas*, 2007; *Golden et al.*, 2008].

[36] Orbicules formed within magmas provide a much weaker analogy, failing comparisons of size, internal structure, context, and mineralogy: the orbicular carbonatite discussed by *Haggerty and Fung* [2006] has orbs made of serpentine + calcite (inferred primary olivine) with radial whiskers or outer shells of ilmenite. The occurrence of these large spherules is also narrowly constrained to occur within a kimberlite dike.

[37] Impact spherules have been described from a number of sedimentary successions on Earth (reviewed by *Simonson and Glass* [2004]). The study of impact spherules in the Early Archean Barberton Greenstone belt (one of the analogs cited by *Knauth et al.* [2005]) provides distinct insight into the nature of impact related deposits [*Krull-Davatzes et al.*, 2006]. In four separate impact events spherules were studied. Mineralogic alteration has occurred, but the inferred primary composition was dominated by glass (now quartz and phyllosilicates). In the well-preserved S3 section, compositional and size gradation was observed in the deposit over small (30 cm) vertical scales. Impact spherules occur in distinct layers; but for Mars, it is not obvious how iron-bearing millimeter-scale impact spherules would have been incorporated into well-sorted sandstones made of much smaller, sulfate-rich grains, much less how they would come to have their observed three-dimensional distribution in Meridiani Outcrop rocks. The Barberton (and other) terrestrial impact spherules also fail mineralogical comparisons: their silicate composition, inference of a glass precursor, and presence of high Cr and Ir are distinctly unlike Meridiani structures. Further, the compositional and stratigraphic zonation in impact spherules point to evolution of chemistry and thermal conditions in the impact plume, and are deposited in section over vertical scales significantly smaller than that traversed by Opportunity. In short, the Barberton example does not match the composition or observed morphology and distribution seen at Meridiani. Similar to Meridiani spherules, though, is the rare presence of concentric interiors. Reports of iron-rich spherules near the Morasko impact site also fail as a Meridiani analog as these small spherules show a wide range of crystallinity from amorphous to highly crystalline and are composed primarily of magnetite [*Stankowski et al.*, 2006].

[38] Of the specific terrestrial spherule analogs proposed to date, only the volcanic examples of *Morris et al.* [2005] are strongly metalliferous. Although these spherules are dominated by hematite ($>90\%$ $\alpha\text{-Fe}_2\text{O}_3$), they are excep-

tionally small (10 to 100 μm). If, however, the interpretation of “microberries” on Mars is born out by future exploration, the Mauna Kea examples are consistent with that size class. The formation of Mauna Kea spherules, through hydrothermal acid sulfate alteration of basaltic tephra is also a reasonable geochemical analog for the inferred starting materials that eventually formed the layered sediments in which the Meridiani spherules are found, (i.e., the dirty evaporate model discussed by *McLennan et al.* [2005] and others). However, large-scale volcanic structures are inconsistent with the observed geomorphology of the Meridiani site. In recent work, *Golden et al.* [2008] have synthesized very small (5–20 μm) hematite spherules with radial structures from hydrothermal acid sulfate (hydronium jarosite) solutions at temperatures of 150° to 200°C.

[39] Another class of metalliferous concretions, found on the seafloor and in lakes, are ferromanganese nodules [*Margolis and Burns*, 1976; *Stiles et al.*, 2001]. Examples include nodules reported from the Baltic Sea, Lake Baikal, Lake Michigan, Lake Ontario, Oneida Lake, and in the deep ocean basin [*Glasby et al.*, 1997; *Takamatsu et al.*, 2000; *Rossmann and Callender*, 1968; *Cronan and Thomas*, 1970; *Moore et al.*, 1980; *Hein et al.*, 1997]. These concretions form at or near the sediment-water interface. They can have a wide variety of shapes, but are commonly spheroidal or discoidal, with spheroidal morphologies maintained via nodule rotation by currents and/or bioturbating organisms on timescales that are fast relative to rates of accretion. Deep ocean nodules are commonly large, up to many centimeters in maximum dimension, but lacustrine examples are often small; Baikal and Lake Michigan examples fall within the mm size range observed at Meridiani. The lacustrine samples are inferred to form quite quickly: 0.02 mm/year [*Rossmann and Callender*, 1968; *Hlawatsch et al.*, 2002]. Ferromanganese nodules are almost always concentrically zoned, in lakes recording the seasonal and annual variability in the development of anoxic conditions at the sediment-water interface, and also the varying influx of metals from offshore sources [*Hlawatsch et al.*, 2002]. The deep ocean nodules likely form from hydrogenetic and diagenetic processes at much slower rates: 0.5 to 15 mm/Ma [*Hein et al.*, 1997]. Metal oxide concentrations typically vary from 20 to 50%, and Fe/Mn ratios vary as well; most marine nodules are dominated by Mn [*Glasby et al.*, 1982]; but examples containing up to 70% $\alpha\text{-Fe}_2\text{O}_3$ have been reported in Lake Michigan [*Rossmann and Callender*, 1968]. Where it has been studied, iron oxide precipitation is coupled to Mn^{4+} reduction, at least partially under microbial influence. These studies point out the strong dependence of composition and growth rate on local water chemistry and sediment influx.

[40] Another terrestrial ferromanganese nodule example is those formed through pedogenic processes [*Stiles et al.*, 2001]. Current depositional models for Meridiani Outcrop rocks involve aeolian transport, with local reworking by surface water [*Grotzinger et al.*, 2005, 2006]. Thus, pedogenic ferromanganese nodules [*Stiles et al.*, 2001] may come closest to a physical analog for Meridiani spherules. Terrestrial nodules occur most frequently in fine-textured soils with restricted permeability. Nodules have been identified in Vertisols (soils with high clay content and volume change potential) since the Tertiary [*Stiles et al.*, 2001, and

references therein]. These terrestrial examples form as Fe- and Mn-hydroxides converting to hematite with dehydration over time. They grow displacively, incorporating surrounding resistant grains, and are well developed in a few thousand years. They are noted to be in the size range of Meridiani spherules and formed within and not on top of enclosing sediments, but the absence at Meridiani of conspicuous interior zonation or abundant manganese discourages too close a comparison.

[41] Partial analogies from several terrestrial settings may provide the best insights into Meridiani spherule formation. Morphological and distributional observations of concretions in sedimentary rocks support the conclusion that Meridiani nodules formed as diagenetic concretions within a sediment column. The hematite spherules in sulfate-rich Hawaiian volcanic rocks indicate the importance of basaltic precursor chemistry, acidic water, and development of crystal orientation during accretion. Independent evidence supports the hypothesis that groundwaters at Meridiani Planum were acidic and conditioned by the chemical weathering of basalts [*Squyres et al.*, 2004b, 2006a]. What is still needed is a process model that explains iron transport through porous sulfate-rich sediments, Fe-oxide nucleation, and precipitation. In mildly acidic to alkaline environments found in most places on Earth, iron transport and deposition is closely tied to redox heterogeneities. In strongly acidic environments, however, ferric iron can be transported aqueously [*Fernandez-Remolar et al.*, 2005; *Alpers et al.*, 1994]. Perhaps critical oversaturation in evaporating groundwaters was all that was required to nucleate iron oxide minerals at dispersed sites within Meridiani sediments. The mechanism could behave similar to an Ostwald ripening process, where numerous initial nucleation sites are redissolved with the constituents moving to and precipitating on larger growing concretions [e.g., *Steefel and van Cappellen*, 1990; *Lasaga*, 1998].

8. Summary and Synthesis

[42] There is diversity in the size and appearance of hematite spherules observed in Meridiani Outcrop rocks, with spherules decreasing and then slightly increasing in size along the traverse route from Endurance to Victoria Crater. Local populations range from submillimeter to several millimeters in diameter. Although distributions appear bimodal in many soil observations, a gradation in size is observed in RAT grind exposures. An additional small diameter (100 μm) size population is possible, but we are not able to confirm this as it lies at the resolution limit of the MI. An increase in aspherical shapes is found near Victoria Crater. In spite of the variation seen in MI, the soil lag is fairly uniform in terms of either the percent area covered as determined from Pancam or through a hematite index or band depth as derived from Mini-TES. These two measures of “blueberry” abundance and cover are roughly correlated, suggesting the major contribution to the Mini-TES signature is from the spherules and not from a more distributed hematite component of the soils. The lack of a 390 cm^{-1} feature in Mini-TES suggests interior concentric, platy or radial structure at scales too fine or with an optical contrast too subtle for MI to observe. Mini-TES does not identify a silicate component in the composition of the

spherules. A contribution from bound water is found in the soils. The dominant size population observed early in the mission in aeolian areas and ripple crests is observed as the primary population in ratted outcrop farther south. This observation suggests that the overlying sediments that have eroded to leave the present lag deposit may have had a population of smaller spherules in addition to the original size distribution seen in Eagle and Endurance craters. This also suggests that the spherules are more resistant to fracture, abrasion and size reduction than was originally thought. It will be interesting, when Opportunity ventures into Victoria Crater, to see if the population gets larger in the sedimentary sequence lower than what has been observed so far.

[43] The Meridiani spherules share some characteristics with many terrestrial examples of spherules. However, no single terrestrial model accounts for (1) the highly uniform, α -Fe₂O₃ dominant composition with high crystallinity, (2) the limited range in size distribution, (3) the predominantly spherical shapes with fused and other forms seen in higher abundance near a larger impact crater, (4) the appearance of two size ranges in a single horizon (Cercedilla), (5) their appearance in large-scale layered sedimentary deposits covering lateral areas of 150,000 km², (6) significant uniformity seen over 10 m of vertical cross section (Endurance Crater), and (7) development of some with adhering outcrop rinds.

[44] The simplest scenario combining elements to explain the observed properties suggests postdepositional or syndepositional spherule formation through groundwater filtration in porous sediments and in response to seasonal temperature, oxygen, or sediment influx changes. Variations in sediment/metal cation influx could also include temporally sporadic volcanic air fall deposition. Temporary shallow basins with underlying saturated ground could have been quite short-lived, perhaps <100 years, and topographically constrained on local scales, with subsequent topographic modification in the following 3.5 Gy. The globally sparse and diverse occurrence of bulk hematite as mapped by TES does not support an impact model as the primary formation mechanism; distributed sites in Valles Marineris and Aram Chaos are also inconsistent with this model [Glotch and Christensen, 2005; Knudson et al., 2007; Weitz et al., 2008]. The occurrence of coarsely crystalline hematite in conjunction with layered sediments at all of these distributed hematite sites also supports the basin/groundwater formation model [Christensen and Ruff, 2004].

9. Conclusions

[45] 1. There is a range of spherule sizes, dominated by two common ranges, less than 1 mm and a few mm. There is possibly a group of very small spherules <100 μ m, but available spatial resolution is inadequate to confirm this. This very small size may correspond to the hematite observed in outcrop by MB. The average size decreases until approximately 1.5 km from Victoria Crater, and then larger sizes again appear in outcrop rocks. Larger sizes near Victoria likely reflect appearance of ejecta blanket from lower-lying stratigraphy, especially at the rock Cercedilla, which is presumed akin to Madrid/Guadarama ejecta

blocks. It should be possible to test this hypothesis as the rover descends into Victoria Crater.

[46] 2. Spherules remain dominantly spherical as observed over the 8 km lateral traverse distance, though unusual shapes and asphericity are more common near Victoria. These features may reflect changes in the diagenetic environment resulting in more fused or merged forms.

[47] 3. Mini-TES senses only the hematite in spherules, not a distributed hematite soil component, and sees no silicate contribution. There is evidence of bound water in soils. Observations are consistent with c-face dominated hematite grains, as either radial, concentric, or random thin plates within the spherules, but on scales below the MI resolution.

[48] 4. No terrestrial analog for spherule formation is consistent with all the observations; the simplest model supports the diagenetic formation of the spherules.

[49] 5. On the basis of terrestrial analogs, hydrothermal conditions are not required to concentrate iron in spherical nodules, but further analysis of terrestrial metalliferous basin and pedogenic concretions is needed to explore the spectral, compositional and zonation similarities of the most iron-oxide-rich examples to those observed at Meridiani.

[50] **Acknowledgments.** This work is supported by the Mars Exploration Project Participating Scientist grant 1243304 to Calvin with additional support from Nevada Space grant and EPSCoR programs. We appreciate the sustained, dedicated participation of the Athena Science team and JPL engineering staff in continued operation and science observations of Spirit and Opportunity.

References

- Alpers, C. N., D. W. Blowes, D. K. Nordstrom, and J. L. Jambor (1994), Secondary minerals and acid mine-water chemistry, in *The Environmental Geochemistry of Sulfide Mine-wastes*, edited by J. L. Jambor and D. W. Blowes, chap. 9, pp. 247–270, Mineral. Assoc. of Can., Quebec, Canada.
- Bandfield, J. L., T. D. Glotch, and P. R. Christensen (2003), Spectroscopic identification of carbonate minerals in the Martian dust, *Science*, 301(5636), 1084–1087, doi:10.1126/science.1088054.
- Bell, J. F., III, et al. (2003), Mars Exploration Rover Athena Panoramic Camera (Pancam) investigation, *J. Geophys. Res.*, 108(E12), 8063, doi:10.1029/2003JE002070.
- Bell, J. F., III, et al. (2004), Pancam multispectral imaging results from the Opportunity Rover at Meridiani Planum, *Science*, 306(5702), 1703–1709, doi:10.1126/science.1105245.
- Bell, J. F., III, J. Joseph, J. N. Sohl-Dickstein, H. M. Arneson, M. J. Johnson, M. T. Lemmon, and D. Savransky (2006), In-flight calibration and performance of the Mars Exploration Rover Panoramic Camera (Pancam) instruments, *J. Geophys. Res.*, 111, E02S03, doi:10.1029/2005JE002444.
- Bishop, J. L., M. D. Dyar, M. D. Lane, and J. F. Banfield (2004), Spectral identification of hydrated sulfates on Mars and comparison with acidic environments on Earth, *Int. J. Astrobiol.*, 3(4), 275–285, doi:10.1017/S1473550405002259.
- Busigny, V., and N. Dauphas (2007), Tracing paleofluid circulations using iron isotopes: A study of hematite and goethite concretions from the Navajo Sandstone (Utah, USA), *Earth Planet. Sci. Lett.*, 254(3–4), 272–287, doi:10.1016/j.epsl.2006.11.038.
- Chan, M. A., B. Beutler, W. T. Parry, J. Ormo, and G. Komatsu (2004), A possible terrestrial analogue for haematite concretions on Mars, *Nature*, 429(6993), 731–773, doi:10.1038/nature02600.
- Chan, M. A., B. B. Bowen, W. T. Parry, J. Ormo, and G. Komatsu (2005), Red rock and red planet diagenesis: Comparisons of Earth and Mars concretions, *GSA Today*, 15(8), 4–10.
- Christensen, P. R., and S. W. Ruff (2004), Formation of the hematite-bearing unit in Meridiani Planum: Evidence for deposition in standing water, *J. Geophys. Res.*, 109, E08003, doi:10.1029/2003JE002233.
- Christensen, P. R., et al. (2000), Detection of crystalline hematite mineralization on Mars by the Thermal Emission Spectrometer: Evidence for near-surface water, *J. Geophys. Res.*, 105, 9623–9642, doi:10.1029/1999JE001093.

- Christensen, P. R., et al. (2004), Mineralogy at Meridiani Planum from the Mini-TES experiment on the Opportunity Rover, *Science*, 306(5702), 1733–1739, doi:10.1126/science.1104909.
- Cronan, D. S., and R. L. Thomas (1970), Ferromanganese concretions in Lake Ontario, *Can. J. Earth Sci.*, 7, 1346–1349.
- Farrand, W. H., et al. (2007), Visible and near-infrared multispectral analysis of rocks at Meridiani Planum, Mars, by the Mars Exploration Rover Opportunity, *J. Geophys. Res.*, 112, E06S02, doi:10.1029/2006JE002773.
- Fernandez-Remolar, D. C., R. V. Morris, J. E. Gruener, R. Amils, and A. H. Knoll (2005), The Rio Tinto basin, Spain: Mineralogy, sedimentary geobiology, and implications for interpretation of outcrop rocks at Meridiani Planum, Mars, *Earth Planet. Sci. Lett.*, 240(1), 149–167, doi:10.1016/j.epsl.2005.09.043.
- Glasby, G. P., P. Stoffers, A. Sioulas, T. Thijssen, and G. Friedrich (1982), Manganese nodule formation in the Pacific Ocean: A general theory, *Geo-Mar. Lett.*, 2(1–2), 47–53, doi:10.1007/BF02462799.
- Glasby, G. P., E. M. Emelyanov, V. A. Zhamoïda, G. N. Baturin, T. Leipe, R. Bahlo, and P. Bonacker (1997), Environments for formation of ferromanganese concretions in the Baltic Sea: A critical review, in *Manganese Mineralization: Geochemistry and Mineralogy of Terrestrial and Marine Deposits*, edited by K. Nicholson et al., *Geol. Soc. Spec. Publ.*, 119, 213–237.
- Glotch, T. D., and J. L. Bandfield (2006), Determination and interpretation of surface and atmospheric Miniature Thermal Emission Spectrometer spectral end-members at the Meridiani Planum landing site, *J. Geophys. Res.*, 111, E12S06, doi:10.1029/2005JE002671.
- Glotch, T. D., and P. R. Christensen (2005), Geologic and mineralogic mapping of Aram Chaos: Evidence for a water-rich history, *J. Geophys. Res.*, 110, E09006, doi:10.1029/2004JE002389.
- Glotch, T. D., P. R. Christensen, and T. G. Sharp (2006), Fresnel modeling of hematite crystal surfaces and application to Martian hematite spherules, *Icarus*, 181(2), 408–418, doi:10.1016/j.icarus.2005.11.020.
- Golden, D. C., D. W. Ming, R. V. Morris, and T. G. Graff (2008), Hydrothermal synthesis of hematite spherules and jarosite: Implications for diagenesis and hematite spherule formation in sulfate outcrops at Meridiani Planum, Mars, *Am. Min.*, 93(8–9), 1201–1214.
- Grotzinger, J. P., et al. (2005), Stratigraphy and sedimentology of a dry to wet eolian depositional system, Burns formation, Meridiani Planum, Mars, *Earth Planet. Sci. Lett.*, 240(1), 11–72, doi:10.1016/j.epsl.2005.09.039.
- Grotzinger, J., et al. (2006), Sedimentary textures formed by aqueous processes, Erebus Crater, Meridiani Planum, Mars, *Geology*, 34(12), 1085–1088, doi:10.1130/G22985A.1.
- Haggerty, S. E., and A. Fung (2006), Orbicular oxides in carbonatitic kimberlites, *Am. Mineral.*, 91(10), 1461–1472, doi:10.2138/am.2006.2194.
- Hein, J. R., A. Koschinsky, P. Halback, F. T. Manheim, M. Bau, J.-K. Kang, and N. Lubick (1997), Iron and manganese oxide mineralization in the Pacific, in *Manganese Mineralization: Geochemistry and Mineralogy of Terrestrial and Marine Deposits*, edited by K. Nicholson et al., *Geol. Soc. Spec. Publ.*, 119, 123–128.
- Hlawatsch, S., T. Neumann, C. M. G. van den Berg, M. Kersten, J. Harff, and E. Suess (2002), Fast-growing, shallow-water ferro-manganese nodules from the western Baltic Sea: Origin and modes of trace element incorporation, *Mar. Geol.*, 182(3–4), 373–387, doi:10.1016/S0025-3227(01)00244-4.
- Jolliff, B. L., and the Athena Science Team (2005), Composition of Meridiani hematite-rich spherules: A mass-balance mixing-model approach, *Lunar Planet. Sci.*, (XXXVI), Abstract 2269.
- Jolliff, B. L., R. Gellert, and D. W. Mittlefehldt (2007a), More on the possible composition of the Meridiani hematite-rich concretions, *Lunar Planet. Sci.*, XXXVIII, Abstract 2279.
- Jolliff, B. L., B. C. Clark, D. W. Mittlefehldt, and R. Gellert, and the Athena Science Team (2007b), Compositions of spherules and rock surfaces at Meridiani, in *Seventh International Conference on Mars*, abstract 3374, Jet Propul. Lab., Pasadena, Calif.
- Klingelhöfer, G., et al. (2004), Jarosite and hematite at Meridiani Planum from Opportunity's Mössbauer spectrometer, *Science*, 306, 1740–1745, doi:10.1126/science.1104653.
- Knauth, L. P., D. M. Burt, and K. H. Wohletz (2005), Impact origin of sediments at the opportunity landing site on Mars, *Nature*, 438(7071), 1123–1128, doi:10.1038/nature04383.
- Knoll, A. H., et al. (2005), An astrobiological perspective on Meridiani Planum, *Earth Planet. Sci. Lett.*, 240(1), 179–189, doi:10.1016/j.epsl.2005.09.045.
- Knoll, A. H., et al. (2008), Veneers, rinds, and fracture fills: Relatively late alteration of sedimentary rocks at Meridiani Planum, Mars, *J. Geophys. Res.*, 113, E06S16, doi:10.1029/2007JE002949.
- Knudson, A. T., R. E. Arvidson, P. R. Christensen, S. L. Murchie, J. F. Mustard, L. H. Roach, C. M. Weitz, and S. M. Wiseman (2007), Aqueous geology in Valles Marineris: New insights in the relationship of hematite and sulfates from CRISM and HiRISE, in *Seventh International Conference on Mars*, abstract 3370, Jet Propul. Lab., Pasadena, Calif.
- Krull-Davatzes, A. E., D. R. Lowe, and G. R. Byerly (2006), Compositional grading in an similar to 3.24 Ga impact-produced spherule bed, Barberton greenstone belt, South Africa: A key to impact plume evolution, *S. Afr. J. Geol.*, 109(1–2), 233–244, doi:10.2113/gssajg.109.1-2.233.
- Kuzmin, R. O., P. R. Christensen, S. W. Ruff, T. G. Graff, A. T. Knudson, and M. Y. Zolotov (2006), Spatial and temporal variations of bound water content in the Martian soil within the Gusev Crater: Preliminary results of the TES and Mini-TES data analysis, *Lunar and Planetary Science Conf.*, 37, 1673.
- Lane, M. D., R. V. Morris, S. A. Mertzman, and P. R. Christensen (2002), Evidence for platy hematite grains in Sinus Meridiani, Mars, *J. Geophys. Res.*, 107(E12), 5126, doi:10.1029/2001JE001832.
- Lane, M. D., M. D. Dyar, and J. L. Bishop (2004), Spectroscopic evidence for hydrous iron sulfate in the Martian soil, *Geophys. Res. Lett.*, 31, L19702, doi:10.1029/2004GL021231.
- Lasaga, A. C. (1998), *Kinetic Theory in Earth Sciences*, 811 pp., Princeton Univ. Press, Princeton, N. J.
- Margolis, S. V., and R. G. Burns (1976), Pacific deep-sea manganese nodules: Their distribution, composition, and origin, *Annu. Rev. Earth Planet. Sci.*, 4, 229–263, doi:10.1146/annurev.ea.04.050176.001305.
- McBride, E. F., and K. L. Milliken (2006), Giant calcite-cemented concretions, Dakota Formation, central Kansas, USA, *Sedimentology*, 53(5), 1161–1179.
- McBride, E. F., A. Abdel-Wahab, and A. R. M. El-Younsy (1999), Origin of spheroidal chert nodules, Drunka Formation (Lower Eocene), Egypt, *Sedimentology*, 46(4), 733–755, doi:10.1046/j.1365-3091.1999.00253.x.
- McBride, E. F., M. D. Picard, and K. L. Milliken (2003), Calcite-cemented concretions in Cretaceous sandstone, Wyoming and Utah, USA, *J. Sediment. Res.*, 73(3), 462–483, doi:10.1306/111602730462.
- McLennan, S. M., et al. (2005), Provenance and diagenesis of the evaporite-bearing Burns formation, Meridiani Planum, Mars, *Earth Planet. Sci. Lett.*, 240(1), 95–121, doi:10.1016/j.epsl.2005.09.041.
- Milliken, R. E., J. F. Mustard, F. Poulet, D. Jouglet, J.-P. Bibring, B. Gondet, and Y. Langevin (2007), Hydration state of the Martian surface as seen by Mars Express OMEGA: 2. H₂O content of the surface, *J. Geophys. Res.*, 112, E08S07, doi:10.1029/2006JE002853.
- Moore, W. S., W. E. Dean, S. Krishnaswami, and D. V. Borole (1980), Growth-rates of manganese nodules in Oneida Lake, New York, *Earth Planet. Sci. Lett.*, 46(2), 191–200, doi:10.1016/0012-821X(80)90005-9.
- Morris, R. V., et al. (2005), Hematite spherules in basaltic tephra altered under aqueous, acid-sulfate conditions on Mauna Kea volcano, Hawaii: Possible clues for the occurrence of hematite-rich spherules in the Burns formation at Meridiani Planum, Mars, *Earth Planet. Sci. Lett.*, 240(1), 168–178, doi:10.1016/j.epsl.2005.09.044.
- Morris, R. V., et al. (2006), Mössbauer mineralogy of rock, soil, and dust at Meridiani Planum, Mars: Opportunity's journey across sulfate-rich outcrop, basaltic sand and dust, and hematite lag deposits, *J. Geophys. Res.*, 111, E12S15, doi:10.1029/2006JE002791.
- Pitman, K. M., J. L. Bandfield, and M. J. Wolff (2006), MGS-TES phase effects and the thermal infrared directional emissivity field measurements of Martian analog sites, *Proc. Lunar Planet. Sci. Conf.*, 37, abstract 1336.
- Raiswell, R., and Q. J. Fisher (2000), Mudrock-hosted carbonate concretions: A review of growth mechanisms and their influence on chemical and isotopic composition, *Geol. Soc. London J.*, 157, 239–251.
- Rieder, R., et al. (2004), Chemistry of rocks and soils at Meridiani Planum from the Alpha Particle X-Ray Spectrometer, *Science*, 306(5702), 1746–1749, doi:10.1126/science.1104358.
- Rogers, A. D., and O. Aharonson (2008), Mineralogical composition of sands in Meridiani Planum determined from Mars Exploration Rover data and comparison to orbital measurements, *J. Geophys. Res.*, 113, E06S14, doi:10.1029/2007JE002995.
- Rossmann, R., and E. Callender (1968), Manganese nodules in Lake Michigan, *Science*, 162, 1123–1124, doi:10.1126/science.162.3858.1123.
- Ruff, S. W., P. R. Christensen, D. L. Blaney, W. H. Farrand, J. R. Johnson, J. R. Michalski, J. E. Moersch, S. P. Wright, and S. W. Squyres (2006), The rocks of Gusev Crater as viewed by the Mini-TES instrument, *J. Geophys. Res.*, 111, E12S18, doi:10.1029/2006JE002747.
- Salisbury, J. W., L. S. Walter, N. Vergo, and D. M. D'Aria (1991), *Infrared (2.1–25 μ m) Spectra of Minerals*, 267 pp., Johns Hopkins Univ. Press, Baltimore, Md.
- Simonson, B. M., and B. P. Glass (2004), Spherule layers: Records of ancient impacts, *Annu. Rev. Earth Planet. Sci.*, 32, 329–361, doi:10.1146/annurev.earth.32.101802.120458.
- Smith, M. D., M. J. Wolff, N. Spanovich, A. Ghosh, D. Banfield, P. R. Christensen, G. A. Landis, and S. W. Squyres (2006), One Martian year of atmospheric observations using MER Mini-TES, *J. Geophys. Res.*, 111, E12S13, doi:10.1029/2006JE002770.

- Soderblom, L. A., et al. (2004), Soils of Eagle Crater and Meridiani Planum at the Opportunity Rover landing site, *Science*, 306(5702), 1723–1726, doi:10.1126/science.1105127.
- Squyres, S. W., et al. (2003), Athena Mars Rover science investigation, *J. Geophys. Res.*, 108(E12), 8062, doi:10.1029/2003JE002121.
- Squyres, S. W., et al. (2004a), The Opportunity Rover's Athena science investigation at Meridiani Planum, Mars, *Science*, 306(5702), 1698–1703, doi:10.1126/science.1106171.
- Squyres, S. W., et al. (2004b), In situ evidence for an ancient aqueous environment at Meridiani Planum, Mars, *Science*, 306(5702), 1709–1714, doi:10.1126/science.1104559.
- Squyres, S. W., et al. (2006a), Two years at Meridiani Planum: Results from the Opportunity Rover, *Science*, 313(5792), 1403–1407, doi:10.1126/science.11130890.
- Squyres, S. W., et al. (2006b), Overview of the Opportunity Mars Exploration Rover mission to Meridiani Planum: Eagle Crater to Purgatory ripple, *J. Geophys. Res.*, 111, E12S12, doi:10.1029/2006JE002771.
- Stankowski, W. T. J., A. Katrusiak, and A. Budzianowski (2006), Crystallographic variety of magnetic spherules from Pleistocene and Holocene sediments in the Northern foreland of Morasko-Meteorite Reserve, *Planet. Space Sci.*, 54(1), 60–70, doi:10.1016/j.pss.2005.08.005.
- Steefel, C. I., and P. van Cappellen (1990), A new kinetic approach to modeling water-rock interaction: The role of nucleation, precursors, and Ostwald ripening, *Geochim. Cosmochim. Acta*, 54, 2657–2677, doi:10.1016/0016-7037(90)90003-4.
- Stiles, C. A., C. I. Mora, and S. G. Driese (2001), Pedogenic iron-manganese nodules in Vertisols: A new proxy for paleoprecipitation?, *Geology*, 29(10), 943–946, doi:10.1130/0091-7613(2001)029<0943:PIMNIV>2.0.CO;2.
- Takamatsu, T., T. Kawai, and M. Nishikawa (2000), Elemental composition of short sediment cores and ferromanganese concretions from Lake Baikal, in *Lake Baikal A Mirror in Time and Space for Understanding Global Change Processes*, edited by K. Minoura, pp. 155–164, Elsevier, New York.
- Weitz, C. M., R. C. Anderson, J. F. Bell, W. H. Farrand, K. E. Herkenhoff, J. R. Johnson, B. L. Jolliff, R. V. Morris, S. W. Squyres, and R. J. Sullivan (2006), Soil grain analyses at Meridiani Planum, Mars, *J. Geophys. Res.*, 111, E12S04, doi:10.1029/2005JE002541.
- Weitz, C. M., M. D. Lane, M. Staid, and E. Noe Dobrea (2008), Gray hematite distribution and formation in Ophir and Candor chasmata, *J. Geophys. Res.*, 113, E02016, doi:10.1029/2007JE002930.
- R. E. Arvidson and B. L. Jolliff, Department of Earth and Planetary Sciences, Washington University, Campus Box 1169, One Brookings Drive, St. Louis, MO 63130-4899, USA.
- J. F. Bell III and S. W. Squyres, Department of Astronomy, Cornell University, 610 Space Sciences Building, Ithaca, NY 14853-6801, USA.
- W. M. Calvin, J. M. Pockock, J. D. Shoffner, and S. D. Thompson, Department of Geological Sciences and Engineering, University of Nevada, M.S. 172, Reno, NV 89557-0138, USA. (wcalvin@unr.edu)
- P. R. Christensen and A. T. Knudson, Department of Geological Sciences, Arizona State University, P.O. Box 876305, Tempe, AZ 85287-1404, USA.
- P. A. de Souza Jr., Tasmanian ICT Center, CSIRO, Hobart, Tas 7000, Australia.
- W. H. Farrand, Space Science Institute, 4750 Walnut Street, Suite 205, Boulder, CO 80301-2532, USA.
- T. D. Glotch, S. M. McLennan, and A. D. Rogers, Department of Geosciences, State University of New York at Stony Brook, Earth and Space Sciences Building, Stony Brook, NY 11794-2100, USA.
- K. E. Herkenhoff and J. R. Johnson, U.S. Geological Survey, 2255 North Gemini Drive, Flagstaff, AZ 86001-1698, USA.
- A. H. Knoll, Department of Organismic and Evolutionary Biology, Harvard University, 26 Oxford Street, Cambridge, MA 02138-2902, USA.
- C. M. Weitz, Planetary Science Institute, 1700 East Fort Lowell Road, Suite 106, Tucson, AZ 85719-2395, USA.